# Effect of the Accretion and Core definition on the Star Formation Rate per Free Fall Time

by

**Fabián Quesada Zúñiga**

Thesis submitted in partial fullfillment of the requirements for the degree of

**MAESTRO EN CIENCIAS en la especialidad de ASTROFÍSICA**

at the

**Instituto Nacional de Astrofísica, Óptica y Electrónica**
August 2023
Tonantzintla, Puebla

Advised by:

**PhD. Manuel Zamora Avilés**
INAOE

# Abstract

Recently, there has been an increasing interest in studying the mass accretion from filaments to clumps and cores within molecular clouds, and their effects on the star formation efficiency (SFE). A common parameter used to characterize the SFE is the *star formation efficiency per free-fall time* ($\epsilon_{ff}$), defined as the fraction of gas converted into stars over a free-fall time ($\tau_{ff}$). Here we present simplified simulations of the gravitational collapse of an isolated core, varying the initial number density ($n_0$ = 100 and 1000 cm$^{-3}$) and considering open/closed boundary conditions (BCs) to allow/disallow accretion onto the numerical box. We define the core as the gas above some density threshold. The simulations start with a slight overdensity at the center of the numerical box and develop a power-low density profile, $n \propto r^{-p}$ (with $p \sim 1.7$), as a consequence of gravitational collapse, forming eventually a sink particle at the center of the core.

Our results show that both, the BCs and the core definition, can affect the measured physical properties of the core and, consequently, the values of the SFE. We find that simulations with low mean densities ($n_0$ $\sim$100 cm$^{-3}$) are more sensitive to the changes in the BCs (with the open boundaries allowing more accretion in the cores than the closed boundaries), while simulations with $n_0$ $\sim$1000 cm$^{-3}$ maintain similar accretion rates onto the core and sink particles regardless of the boundaries. We also notice a constancy of $\epsilon_{ff}$ in space and time, as suggested by recent observations. This can be interpreted as a consequence of the result that a collapsing region with a stationary density profile $r^{-2}$ has a value of $\epsilon_{ff}$ that is independent of radius and time.

# Resumen

Recientemente, ha habido un mayor interés en estudiar el acrecimiento de masa desde filamentos a núcleos dentro de nubes moleculares, y sus efectos en la eficiencia de formación estelar (SFE). Un parámetro comúnmente utilizado para caracterizar la SFE es la *eficiencia de formación estelar por tiempo de caída libre* ($\epsilon_{ff}$), definida como la fracción de gas convertida en estrellas durante un tiempo de caída libre ($\tau_{ff}$). En este trabajo presentamos simulaciones simplificadas de colapso gravitacional de un núcleo aislado, variando la densidad inicial ($n_0$ = 100 y 1000 cm$^{-3}$) y considerando condiciones de frontera abiertas/cerradas (BCs) para permitir/denegar el acrecimiento dentro del dominio numérico. Definimos el núcleo como el gas por encima de cierto umbral de densidad. Las simulaciones comienzan con una ligera sobredensidad en el centro de la caja numérica y desarrollan un perfil de densidad de ley de potencias, $n \propto r^{-p}$ (con $p \sim 1.7$), como consecuencia del colapso gravitacional, formando finalmente una partícula *sink* en el centro del núcleo.

Nuestros resultados muestran que tanto las BCs como la definición del núcleo pueden afectar las propiedades físicas medidas del núcleo y, por tanto, los valores de la SFE. Encontramos que las simulaciones con densidades medias bajas ($n_0$ ∼100 cm$^{-3}$) son más sensibles a los cambios en las BCs (las abiertas permitiendo un mayor acrecimiento en los núcleos que las cerradas), mientras que las simulaciones con $n_0$ ∼1000 cm$^{-3}$ mantienen tasas de acrecimiento similares hacia el núcleo y las partículas *sink* independiente de las fronteras. También observamos una constancia de $\epsilon_{ff}$ en el espacio y el tiempo, como sugieren observaciones recientes. Esto puede interpretarse como una consecuencia del resultado de que una región en colapso con un perfil de densidad estacionario $r^{-2}$ tiene un valor de $\epsilon_{ff}$ que es independiente del radio y el tiempo.

# Acknowledgment

This thesis has been possible thanks to an scholarship granted by CONAHCYT-México. Additional support was provided by the Laboratorio Nacional de Supercómputo del Sureste de México (LNS), for the computational time to run the simulations. And from the Instituto Nacional de Astrofísica, Óptica y Electrónica (INAOE).

I am also very grateful with my advisor, Dr. Manuel Zamora Avilés, for his guidance and constant support that made possible this thesis project; and to the Dr. Enrique Vázquez Semadeni and Dr. Javier Ballesteros Paredes, for their support and help in this project and their ideas during the realization. I would not have accomplish this without their patience and teachings, both academically and personally.

Finally, I would like to express my heartfelt gratitude to my family and friends who have been unwavering in their support throughout my journey. Your love, encouragement, understanding, and belief in my abilities have been invaluable sources of motivation and made this accomplishment possible. I am truly grateful to have you all by my side.

# Dedicatory

Esta tesis está dedicaca a ...

A mi familia en Costa Rica, por darme la fuerza para venir,
A mi familia en México, por darme la fuerza para quedarme,
A Dani, por darme la fuerza para seguir,
A mí, por no rendirme.

# Contents

# Chapter 1
# Introduction

The interstellar medium (ISM) is the vast and complex space between stars. It is composed of several components, including gas and dust particles, magnetic fields, and cosmic rays. The ISM contains the raw material from which new stars can be formed, so its understanding is crucial to gain insight into the processes that shape the formation and evolution of galaxies, stars, and planets and about the universe's overall structure and evolution.

Important aspects to study about the ISM, and the main focus in this work, are the star formation rate (SFR) and the star formation efficiency (SFE), which are the velocity and efficiency with which stars form in the ISM. A better understanding of these concepts provides insight into the physical processes that drive local star formation (such as the influence of gas dynamics, selfgravity, feedback, etc), and the process in which the star formation regulates itself, since the newborn stars can disperse the parent cloud by feedback processes, preventing the formation of a new generation of stars.

Because this work is mainly focused on the early stages of star formation, a brief explanation of the interstellar gas, with focus on molecular clouds in our galaxy will be given in the following sections.

## 1.1 Interstellar Gas

The interstellar gas is a crucial component of the ISM (being roughly the 10% of the total mass of the Milky Way). It is primarily composed of hydrogen and helium, with other elements less abundant such as carbon, nitrogen, and oxygen (Ferrière, 2001).

| Parameters | Phases | | | | |
|---|---|---|---|---|---|
| | Cold | | Warm | | Hot |
| | Subphases | | | | |
| | CNM | MC | WNM | DIG | HIM |
| $n$ (cm$^{-3}$) | $20 - 50$ | $10^2 - 10^6$ | $0.2 - 0.5$ | $0.2 - 0.5$ | $10^{-4} - 10^{-2}$ |
| $T$ (K) | $50 - 100$ | $10 - 20$ | $6000 - 10000$ | $\sim 8000$ | $\sim 10^6$ |
| $\%V$ | $1 - 4$ | $1 - 2$ | $10 - 20$ | $20 - 50$ | $40 - 70$ |
| $M(10^9$ M$_\odot)$ | $\sim 1.5$ | $\sim 2$ | $\sim 1.5$ | $\sim 1$ | $\sim 0.1$ |

Table 1.1: Characteristics of the ISM gas subphases within the Milky Way, adapted from Draine (2011). From left to right, each subphase corresponds to cold neutral medium (CNM), molecular clouds (MC), warm neutral medium (WNM), diffuse ionized gas (DIG) and hot ionized medium (HM). From top to bottom, the physical parameters showed are: number density ($n$), temperature ($T$), volume percentage of the galaxy ($\%V$) and total mass ($M$).

This gas is most commonly characterized in three phases: the cold phase which is made up of molecular and atomic hydrogen gas as well as dust; the warm phase which consists of both atomic and ionized hydrogen gas; and the hot phase which contains shocked gas from supernova explosions and coronal gas. Table 1.1 presents more specific physical parameters and characteristics about these phases.

The ISM has other components besides gas, such as dust, magnetic fields and cosmic rays. The dust corresponds to nearly 1% of the ISM mass (with gas being the 99% left), it has typical sizes of $\sim 0.1$ mm, is composed mostly by silicates and graphite, and is the main responsible for the interstellar extinction. The magnetic fields are present in every phase of the ISM, and, because of the magnetic structure they provide to the gas and dust, seem to be responsible for reducing the SFR (in a factor of $\sim 2-3$) and shaping the interstellar gas. Finally, cosmic rays consist of high energy particles that work as a heating mechanism in the ISM, especially in denser regions within molecular clouds (Estalella & Anglada (1999), Federrath (2015)).

Since in this work we are interested on the process of star formation, we will focus in the following section on the cold phase of the ISM, specifically on the molecular component.

## 1.2 Molecular Clouds

The molecular gas in the ISM (i.e., the gas composed primarily of molecular hydrogen, $H_2$, with traces of other molecules) is mainly concentrated in high density *clouds*. These *clouds* are called molecular clouds (MCs) and are the places where the star formation process takes place as a result of the gravitational collapse of their densest regions (e.g., Shu et al., 1987).

The average physical properties of MCs are present in Table 1.1. However, MCs are not regular and well-defined entities, instead they have complex substructures often described as filamentary, hierarchical or fractal (e.g., Falgarone et al., 1991).

### 1.2.1 Substructures of MCs: filaments, clumps, and cores.

In the astrophysics community, there is a consensus on the morphological and physical properties of MCs. Here, we will focus on the more common: filaments, clumps and cores.

Filaments are elongated structures with an aspect ratio larger than 5, and significantly overdense compared to their surroundings ($\sim$ 2 orders of magnitude). These structures are observed typically in CO molecular line emission or dust extinction as a network of filamentary structures. Observational evidence suggest that the formation of these structures precedes the star formation itself in inner substructures (clumps and cores; see, e.g., André et al., 2014, and references therein).

Inside these filaments, other nested structures are defined: clumps and dense cores, both being individual fragments or local overdensities which correspond to local minima in the gravitational potential field of a molecular cloud. In general, a clump and a core are characterized by their physical properties, as a clump presents average number densities of $n \sim 10^3 - 10^4$ cm$^{-3}$ and sizes of $L \sim 0.1 - 2$ pc, while the cores have number densities of $n \geq 10^4$ cm$^{-3}$ and sizes of $L \leq 0.1$ pc (e.g., Chevance et al., 2022, and Table 1.2), these latter objects usually show radial density profiles with the form $n \propto r^{-p}$ where $p \sim 2$ with some deviations (see Figure 1.1 and Section 2.2.3).

Cores are typically detected as the immediate vicinity of a local maximum in observed column density maps. Transitions of some molecules are used to trace dense gas, some examples are the $^{13}$CO, $NH_3$ or $N_2H^+$ molecules (Pillai et al. (2006), André

| MCs Substructures | Physical Parameters | | |
|---|---|---|---|
| | $n$ [cm$^{-3}$] | $L$ [pc] | $T$ [K] |
| Clump | $10^3 - 10^4$ | $0.1 - 2$ | $\sim 10$ |
| Low-density Core | $10^4 - 10^5$ | $\leq 0.1$ | $\sim 10$ |
| High-density Core | $\geq 10^5$ | $\leq 0.1$ | $\sim 10$ |

Table 1.2: Physical parameters of some substructures defined within molecular clouds (André et al. (2014), Chevance et al. (2022)), where $n$ is the number density, $L$ is the size, and $T$ is the temperature.

et al. (2014)). In numerical models, on the other hand, a threshold in mass density is commonly used, and depending on the value of this threshold density, filaments, clumps or cores can be defined within the 3D density field in the numerical domain in accordance with the observational data (see for example, the methodology in Camacho et al. (2020)).

It is important to note that each molecular tracer is excited at different densities and temperatures and therefore delineates structures with different extents. As a result, there is no single tracer or threshold density that can be used to distinguish all different substructures within MCs. The criteria used to define some of these regions (filaments, clumps, and cores) are therefore conventional but ambiguous. In reality, MCs are a density continuum, where certain substructures defined by the chosen observed tracer are separated for convenience (although these substructures are not real objects). Study these regions with numerical simulations allow us to analyze their evolution during the early states up to the time of star formation.

## 1.3 Star Formation Efficiency

The SFE is an observable that models and simulations try to explain and is influenced by both spatial and temporal factors. Traditionally, SFE assumes that a MC is a particular and finite gas reservoir with a well-defined lifespan and mass. However, recent studies from observations and theoretical models indicate that these assumptions may not always be true. Instead, MCs can accrete fresh gas from an atomic envelope (Molinari et al., 2014). This situation makes the understanding of the SFE

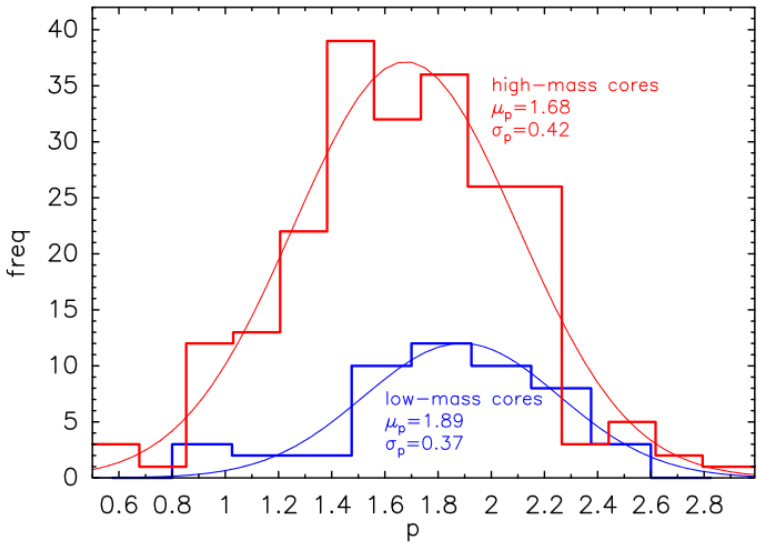


Figure 1.1: Histogram of different observational data from dense cores undergoing star formation, showing the distribution of slopes ($p$) of the density profile ($n \propto r^{-p}$). The blue histogram shows low-mass cores (with typical sample sizes of 0.002-0.2 pc) and the red histogram show high-mass cores (with typical sample sizes of 0.1-1 pc). Thin curves are Gaussian fits. Finally, the position of the peak $\mu_p$ and the standard deviation $\sigma_p$ are annotated. Image taken from Gómez et al. (2021).

as an elusive concept, as the gas accreted by stars comes from large distances[1] to reach the sites of star formation.

### 1.3.1 Instantaneous Star Formation Efficiency

The *Instantaneous* Star Formation Efficiency (SFE, for the purposes of this work) is the mass fraction of gas that is converted into stars at a given time $t$, so

$$\mathrm{SFE}(t) = \frac{M_\star}{M_\mathrm{c} + M_\star}, \tag{1.3.1}$$

where $M_\star$ is the mass in stars within the region of study and $M_\mathrm{c}$ the cloud mass. Because this value evolves in time through the lifetime of the region, it is expected that SFE $\to$ 1 in evolved regions where the all the gas is consumed in forming

[1]The core accretes its mass from the filament surrounding it. In a dynamical scenario, this material comes from large distances throughout the filament Gómez & Vázquez-Semadeni (2014).

stars. Although, newborn stars ionize and disperse the parent cloud preventing high efficiencies (e.g., Grudić et al., 2019).

Also, the SFE value depends on the scale of the studied object. Observations show that at scale of the whole GMC SFE$\sim$2% (e.g., Myers et al., 1986), whereas in dense (massive star forming) cores SFE$\sim$30-50% (e.g., Lada & Lada, 2003).

### 1.3.2 Star Formation Efficiency per Free-Fall Time

The star formation efficiency per free-fall time ($\epsilon_{ff}$, also commonly named star formation rate per free-fall time) is the fraction of a GMC (or any substructure) that is turned into stars in a free-fall time. This parameter was first introduced by Krumholz & McKee (2005), and is defined as

$$\epsilon_{ff} = \frac{\dot{M}_\star}{M_\mathrm{c}} \langle \tau_{ff} \rangle, \tag{1.3.2}$$

where $\dot{M}_\star$ is the SFR, and $\langle \tau_{ff} \rangle$ is the mean free-fall time (see Section 2.2.1). It has been suggested that for a structure in gravitational free-fall collapse, a value of $\epsilon_{ff} \approx 1$ is expected (e.g., Krumholz et al., 2019).

The measurement of this parameter in observations has some constrains that may affect its value. For example, the most reliable approach for the estimation of $\epsilon_{ff}$ in resolved (closed) MCs computes the SFR by counting young stellar objects (YSOs); this method is limited by the sensibility of the telescopes (e.g. *Spitzer*) and is only available for the solar neighborhood (farther regions must make a correction for the unseen part of the Initial Mass Function). The gas mass and mass density (needed to calculate the free-fall time) is estimated from the column density map, assuming that the third dimension along the line of sight is comparable in size with the two observed in the sky plane (e.g., Ochsendorf et al., 2017; Pokhrel et al., 2021).

In general, there is consensus in a canonical value of $\epsilon_{ff} \simeq 0.006 - 0.026$ for regions $\gtrsim$ 1 pc, but with dispersion of at least one order of magnitude above and below this range (see a recent review by Krumholz et al., 2019). The left panel in Figure 1.2 shows a compilation of different works that illustrate this consensus in molecular objects with different densities (from MCs as whole to dense cores). The right panel shows a constant $\epsilon_{ff}$ behavior in observations around 0.026 for a sample

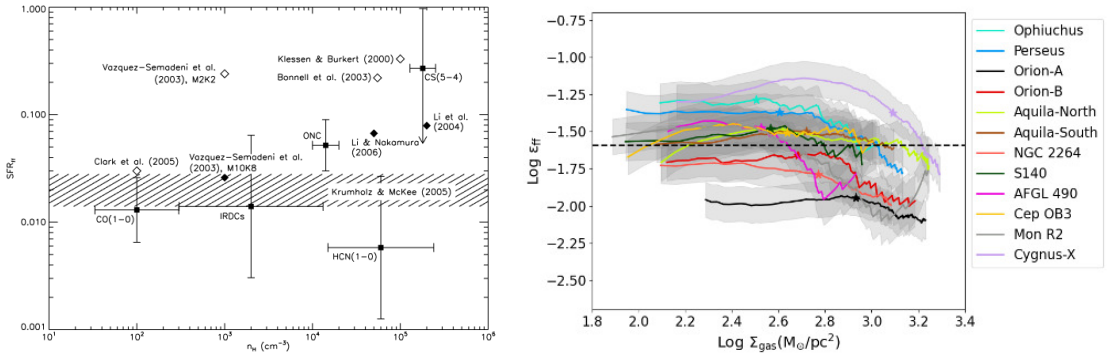


Figure 1.2: *Left panel*: Plot of $\epsilon_{ff}$ ($\mathrm{SFR}_{ff}$ in this figure) versus the characteristic density of a given region $n_H$. Every data comes from different observational and numerical works, referenced in the image itself. The filled squares with error bars are observational estimates, open diamonds are from turbulent numerical simulations, and the horizontal bar is the analytic prediction by Krumholz & McKee (2005, $\epsilon_{ff} \sim 0.01 - 0.02$). Figure taken from Krumholz & Tan (2007). *Right panel*: Variation of $\epsilon_{ff}$ with the surface density for a sample of nearby clouds. The dashed line corresponds to the median of $\epsilon_{ff} \sim 0.026$. Figure taken from Pokhrel et al. (2021).

of nearby MCs, where each cloud has a different evolutionary state, and still, they all have similar $\epsilon_{ff}$ values; also, the range of surface densities ($\Sigma_{\mathrm{gas}}$) within a given cloud can be interpreted as a range in size of the contours used to calculate $\Sigma_{\mathrm{gas}}$, and in every cloud the $\epsilon_{ff}$ remains mostly constant throughout this horizontal axis ($\Sigma_{\mathrm{gas}}$ or size).

As this is a surprisingly low value, different theoretical models try to explain it. Turbulent numerical simulations, with self-gravity and magnetic fields, find reasonable values ($\epsilon_{ff} \sim 0.04$) only when feedback processes (outflows) are taken into account (see, e.g., Federrath, 2015) when considering unrealistic large levels of turbulence (e.g., Padoan et al., 2012; Kim et al., 2021). Other models, where turbulence decays and gravity drives the evolution collapsing the cloud and forming stars, produce reasonable values of $\epsilon_{ff}$ considering feedback effects (such as outflows and ionizing radiation) (e.g., Grudić et al., 2018). However, measurements of these parameters from numerical simulations must be interpreted with caution, as they are measured from the raw simulation data, rather than from synthetic observations. This can lead to inaccuracies, as the raw data may not fully capture the effects of observational

biases.

Finally, note that there is no systematic observations or numerical studies to date that explore the $\epsilon_{ff}$ at scales of dense cores, except for the observational work by Louvet et al. (2014) where they quantified $\epsilon_{ff} \sim 0.1 - 1$ in dense cores of a mini-starburst ridge.

Nowadays, the physical nature of this parameter is highly discussed. The main objective of this work is to study its origin and evolution by performing numerical simulations of a simplified spherical gravitational collapse in order to understand the basic physics (gravity) that could be affecting the behavior of this parameter at scales of dense cores.

.

# Chapter 2

# Gravitational Collapse of dense cores

There are two main models of star formation with opposing assumptions. The *turbulent* model assumes that clouds are turbulent and long-lived, and only overdensities at small scales (dense cores) manage to collapse, thus maintaining the low SFE observed (e.g., Mac Low & Klessen, 2004). On the other hand, the *global hierarchical collapse* (GHC) scenario assumes that clouds can be in a state of global collapse, with the overdensities (cores) collapsing faster than the cloud as a whole and the SFE being regulated by feedback processes (e.g., Vázquez-Semadeni et al., 2019). In any event, in both models, the dense cores contract gravitationally and our results can be valid regardless of the scenario of star formation.

Gravitational collapse occurs when the gravitational energy overwhelms the counteracting processes that tend to keep stable the system (thermal, magnetic, rotational, and turbulent energies), leading to the collapse and accretion of mass.

This chapter delves into the intricacies of gravitational collapse of dense cores, exploring its theoretical foundations and examining various analytical treatments used to study this phenomenon. In this work we will assume cores with spherical symmetry, which is a good first approximation but not entirely true as observations show that the cores are slightly elongated (see, e.g., Francesco et al., 2006).

## 2.1 Equilibrium and stability

### 2.1.1 Jeans Analysis

Here we deduce the Jeans Length and Jeans Mass using the virial theorem (Landau & Lifshits, 2003), which gives us a very close result to the perturbative analysis originally made by Jeans (1902). We must notice that the calculation presented here is a first-order approximation, because we are considering a uniform sphere instead of a sphere with a density profile.

The Virial Theorem states that

$$\frac{1}{2}\frac{d^2I}{dt^2} - 2K = \left(2U - \oint_S P\boldsymbol{x}\cdot d\boldsymbol{S}\right) + \left(\mathcal{M} + \oint_S \boldsymbol{x}\cdot\mathbf{T}\cdot d\boldsymbol{S}\right) + W, \tag{2.1.1}$$

where $I$ is the moment of inertia, $K$ is the kinetic energy, $U$ is the internal energy, $P$ is the pressure, $\mathcal{M}$ is the magnetic energy, $T$ is the Maxwell's magnetic stress tensor and $W$ is the gravitational energy. By searching for a state of equilibrium between the internal and gravitational energy, we can neglect the terms related to other forces, and we assume virial equilibrium, i.e., $\frac{d^2I}{dt^2} = 0$. We then obtain that the total internal energy is equal to minus half of the total gravitational energy

$$U = -\frac{1}{2}W. \tag{2.1.2}$$

The gravitational energy for a spherical cloud with uniform density can be expressed as

$$W = -\frac{3}{5}\frac{GM^2}{R}, \tag{2.1.3}$$

where $G$ is the gravitational constant, $M$ and $R$ the cloud mass and radius, respectively.

On the other hand, the internal energy can be approximated as

$$U = \frac{3}{2}Nk_BT, \tag{2.1.4}$$

where $N$ is the total number of particles (atoms or molecules) in the cloud, $k_B$ is

the Boltzmann constant, and $T$ is the temperature of the gas. For simplicity in the further analysis, $N$ is substituted by $\frac{M}{\mu m_H}$, where the expression $\mu m_H$ corresponds to the average mass per particle.

The cloud mass can also be expressed in terms of its density and radius, so

$$M = \frac{4}{3} G \pi R^3 \rho_0. \tag{2.1.5}$$

These expressions are used in equation 2.1.2 to get the following relation for the radius

$$R^2 = \frac{15}{4\pi} \frac{k_B T}{\mu m_H G \rho_0}. \tag{2.1.6}$$

Now, the sound speed ($c_s$) is introduced for an isothermal gas,

$$c_s^2 = \frac{kT}{\mu m_H}. \tag{2.1.7}$$

Then it is finally obtained

$$R = \sqrt{\frac{15}{4\pi} \frac{c_s^2}{G\rho_0}} \equiv L_J. \tag{2.1.8}$$

This expression represents the Jeans length ($L_J$). It is the characteristic size of a given cloud that determines its stability against gravitational collapse. Structures with scales larger than $L_J$ are unstable to gravitational collapse, whereas smaller scales are gravitationally stable.

On the other hand, a characteristic value of mass required to induce a collapse can be defined, similarly to $L_J$. By replacing the Jeans length in equation 2.1.5, we obtain

$$M_J = \frac{5}{2} \frac{c_s^3}{G^{3/2} \rho_0^{1/2}} \sqrt{\frac{15}{\pi}}. \tag{2.1.9}$$

Thus, a cloud is gravitationally unstable if its mass is greater than this Jeans mass ($M_J$).

### 2.1.2 Bonnor-Ebert Analysis

The Bonnor-Ebert sphere is a theoretical model that describes a self-gravitating, isothermal gas cloud in hydrostatic equilibrium. It provides insights into the stability and structure of molecular clouds, especially those that are marginally stable and on the verge of collapse (Ebert (1955), Bonnor (1956)).

In the Bonnor-Ebert model, the gas cloud is assumed to be spherically symmetric and in hydrostatic equilibrium, meaning that it is balanced between the inward gravitational force and the outward force due to pressure gradient. This condition is mathematically expressed as

$$\frac{\mathrm{d}P(r)}{\mathrm{d}r} = -\frac{G\rho(r)}{r^2}, \tag{2.1.10}$$

where $P(r)$is the pressure, $\rho(r)$ is the density, and $r$ the radial distance.

In the context of the Bonnor-Ebert spheres, we can solve the equation above using the expression (Clarke & Carswell, 2007)

$$\frac{1}{\xi^2}\frac{d}{d\xi}\left(\xi^2\frac{d\psi}{d\xi}\right) = e^{-\psi}, \tag{2.1.11}$$

where $\psi$ is a non-dimensional variable related to the density as

$$\psi \equiv -\ln\left(\frac{\rho}{\rho_0}\right), \tag{2.1.12}$$

and $\xi$ is a non-dimensional variable related to the radius as

$$\xi \equiv \left(\frac{4\pi G\rho_0}{c_s^2}\right)^{1/2} r. \tag{2.1.13}$$

The density profiles of these spheres vary according to the value of the radius: for small $r$, the profile seems nearly flat, and for larger distances from the center, the profile approximates to $\rho \propto r^{-2}$, known as the Singular Isothermal Solution (SIS),

$$\rho(r) = \frac{c_s^2}{2\pi G r^2}. \tag{2.1.14}$$

An example of a collapse driven initially from a marginally unstable Bonnor-Ebert sphere is shown in the right panel of Figure 2.1. More analysis regarding the SIS as

well as some examples of classical solutions will be explored in Section 2.2.2.

## 2.2 Gravitational Collapse

### 2.2.1 Free-fall Time

Understanding the free-fall time is important, as it provides a good approximation of the timescale on which a system will collapse due to selfgravitaty. Its derivation begins by assuming the most simple case of collapse, a spherical mass distribution with uniform density and radius $R$. The sphere is subject only to the gravitational pull of the mass interior to $R$, and no other forces are taken into account.

We begin by taking the equation of motion,

$$-\frac{1}{2}\frac{du^2}{dr} = \frac{GM}{r^2}, \tag{2.2.1}$$

where, again, $M$ is the cloud mass (which will remain constant), and the negative sing in the acceleration is because the velocity $u$ points inward during the collapse. We can integrate this equation with the initial conditions $r(t=0) = R$ and $u(t=0) = 0$, and defining $M(R) = M_0$ and $\rho(t=0) = \rho_0$ as the initial mass and density respectively, to obtain

$$u = -\left[2GM_0\left(\frac{1}{r} - \frac{1}{R}\right)\right]^{1/2}, \tag{2.2.2}$$

because $u(t) = dr/dt$, we can rewrite the previous expression as

$$dt = -\frac{dr}{\left[\frac{2GM_0}{R}\left(\frac{R}{r} - 1\right)\right]^{1/2}}. \tag{2.2.3}$$

At this point, we define the non-dimensional variable $\zeta = r/R$, and noticing that $M_0 = \frac{4}{3}\pi\rho_0 R^3$,

$$dt = -\left(\frac{8\pi G\rho_0}{3}\right)^{-1/2}\left(\frac{\zeta}{1-\zeta}\right)^{1/2} d\zeta. \tag{2.2.4}$$

By integrating this from $r = R$ to $r = 0$, we obtain the final expression

$$\tau_{ff} = \sqrt{\frac{3\pi}{32G\rho_0}}, \tag{2.2.5}$$

which corresponds to the gravitational free-fall time, i.e., the time it takes for the sphere to collapse completely from a radius $R$.

Notice how this parameter only has dependence in density, so all the material would collapse at the same time regardless of the radius. This case is known as *homologous* collapse, and give us a good first approximation of the collapse timescale (e.g., Binney & Tremaine, 1987).

### 2.2.2 Singular Isothermal Solution (SIS)

As mentioned in Section 2.1.2, the singular isothermal solution (SIS) represent an idealized analytical model of gravitational collapse. Although, it does not represent a realistic approach of the physical conditions observed in MCs, since some ingredients that are not taken into account in the analysis are present in the process of star formation, such as turbulence, magnetic fields, etc. However, it is a good instrument to study the initial conditions for gravitational collapse, obtaining interesting implications product of this analysis. In this section, we will briefly discuss two famous and classic solutions of this scenario to better understand the principles of collapse: The *inside-out* solution by Shu (1977) and the *asymptotic* solution by Whitworth & Summers (1985):

#### 2.2.2.1 Asymptotic solutiom (Whitworth & Summers, 1985)

The authors found three solutions for the dimensionless velocity ($\nu(\xi) \equiv u(t,r)/c_s$) and density ($\bar{\rho}(\xi) \equiv 4\pi G t^2 \rho(t,r)$) based on the condition chosen for the variable $\xi$ (see equation 2.1.13) but with a time-dependence (so $\xi \equiv \frac{r}{c_s t}$) as a set of Taylor expansions:

- The *settling solution* (when $\xi \to 0^-$, or $t < 0$):

$$v(\xi) = \frac{2\xi}{3} + O\left(\xi^3\right), \tag{2.2.6}$$

$$\bar{\rho}(\xi) = \bar{\rho}_0 + O\left(\xi^2\right) \tag{2.2.7}$$

- The *freefall solution* (when $\xi \to 0^+$, or $t > 0$):

$$v(\xi) = -\left(\frac{2m_0}{\xi}\right)^{1/2} + O\left(\xi^{1/2}\right), \tag{2.2.8}$$

$$\bar{\rho}(\xi) = \left(\frac{m_0}{2\xi^3}\right)^{1/2} + O\left(\xi^{-1/2}\right) \tag{2.2.9}$$

- The *cruising solution* (when $\xi \to \infty$):

$$v(\xi) = v_\infty - \frac{\bar{\rho}_\infty - 2}{\xi} + O\left(\xi^{-2}\right), \tag{2.2.10}$$

$$\bar{\rho}(\xi) = \frac{\bar{\rho}_\infty}{\xi^2} + O\left(\xi^{-4}\right) \tag{2.2.11}$$

the parameters introduced in those solutions are the following:

- $\bar{\rho}_0$ is the dimensionless central density.
- $m_0$ is the dimensionless central point mass in the late phase of the collapse.
- $v_\infty$ is the dimensionless inflow velocity far from the center.
- $\bar{\rho}_\infty$ is the dimensionless density at some large distance from the center.

To better understand these solutions, a timescale is defined and the time $t = 0$ is chosen to be the time in which a singularity is formed at the center of the sphere (in terms of a star formation system, it represents the moment when a protostar is created), so any negative time describes a *prestellar stage*, and a positive time describes a *protostellar stage*.

These solutions describe different stages and regions of the collapse. The first two (when $|\xi| \to 0$) represent the *inner region* of the sphere (as pointed out by the authors), while the *cruising* solution represents the *outer region*. In the same way, the *settling* solution corresponds to the *prestellar* stage, and the *freefall* solution the *protostellar* stage. Figure 2.1 illustrate all these scenarios and the evolution of $|\xi|$ with $v$ and $\rho$.

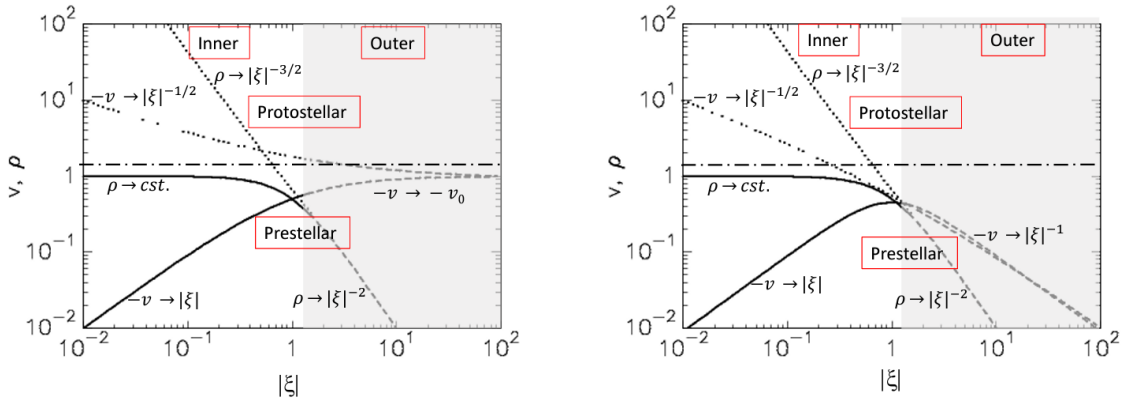


Figure 2.1: Scenarios of the *asymptotic* solution. In both panels, the white area represents the *inner region*, and the shaded area represents the *outer region* (see the text). The dashdotted line approximately separates the *prestellar* stage from the *protostellar* stage. The solid lines indicate the *settling* solution, the dotted lines indicate the *freefall* solution, and finally, the dashed lines indicate the *cruising* solution. The *left panel* shows a case with a finite infall speed at infinity, $v_\infty < 0$, corresponding to a global collapse; and the *right panel* shows a case with vanishing infall speed at large distances, $v_\infty = 0$, corresponding to local collapse. Image taken from Vazquez-Semadeni, in prep.

#### 2.2.2.2 Inside-out solution (Shu, 1977)

This solution assumes that a fully dynamical collapse should start from near-equilibrium configurations, very close to unstable Bonnor-Ebert spheres (see Section 2.1.2). Some arguments given by the author to support the analysis are:

- The $r^{-2}$ profile is an indicator of hydrostatic equilibrium at all radii, as it shows balance between self-gravity and thermal pressure.
- The sound waves are responsible for adjusting the pressure in the region.
- Solutions that imply flows with supersonic velocity connecting smoothly to subsonic velocities are considered unrealistic and unstable configurations.
- Hence, the collapse occurs subsonically everywhere in the sphere.

In general, this solution presents itself as an initial condition for the collapse for the *cruising* solution, specifically when $t \to 0$ and $v_\infty = 0$. Some important situations

must be mentioned about this solution:

- This scenario corresponds exclusively to the protostellar stage, since the author assumes the prestellar stage occurs quasistatically.
- At $t = 0$ the central object (the future star) has $M = 0$, even though there is a density diverging in that position.
- At $t > 0$, the mass of the star increases linearly with time as

$$M_* = \frac{c_s^3 m_0}{G} t, \tag{2.2.12}$$

  so the star would have a constant mass accretion rate as

$$\dot{M}_* = \frac{c_s^3 m_0}{G} \tag{2.2.13}$$

### 2.2.3 Evolution of the density profile

An interesting analysis about the evolution of the density profile during the prestellar stages was developed by Gómez et al. (2021). By assuming that the density profile has the form $r^{-p(t)}$, with $0 < p < 3$, they obtain an expression for the temporal rate of change of the parameter $p(t)$ as

$$\frac{dp}{dt} = \left(3 - \frac{3p}{2}\right) \left[\frac{4\pi G \rho_0 f^2}{3-p}\right]^{1/2} \frac{(r/r_0)^{-p/2}}{-\ln(r/r_0)}, \tag{2.2.14}$$

where $\rho_0$ is the region initial density, $r_0$ is the Jeans Length corresponding to $\rho_0$, and $f$ is a constant that relates the radial flow velocity with the infall speed in the form $v_r = -f v_{ff}$.

Since the authors showed that the prestellar collapse proceeds from the outside-in, they only consider the scenario when $r < r_0$, so the behavior of the parameter (i.e. the sign of the expression) is determined for the expression $\left(3 - \frac{3p}{2}\right)$. Hence, when $p > 2$, the slope decreases, while in $p < 2$ increases at all radii. This shows the nature of the value $p = 2$ as an attractor for other slopes, and the stationary state and radius independence of this scenario.

A scenario with $p \gg 2$ can be neglected, as the $p \sim 2$ profile is considered a natural result of the scale-free gravitational collapse (e.g., Li, 2018), and observations shows that there is highly unlikely to find a core with slope $p > 2.8$ (see Figure 1.1 from Gómez et al., 2021).

The previous analysis means that, with a regular gravitational collapse starting with a density profile characterized with $p \geq 0$, the evolution will lead the slope towards a $p = 2$ behavior.

# Chapter 3

# Numerical Methods

## 3.1 Hydrodynamic equations

Since the gas in the ISM behaves as a fluid, we can use the hydrodynamic equations as a good approximation to understand its dynamics.

For this work, because there are no diffusive effects taken into account, it is easier to study the hydrodynamics by using the Euler equations (Dyson & Williams (1980), Landau & Lifshits (2003)):

- Continuity equation: this expresses the conservation of mass of a fluid element (or gas parcel),

$$\frac{\partial \rho}{\partial t} + \nabla \cdot (\rho \mathbf{u}) = 0, \tag{3.1.1}$$

  where $\rho$ and $\mathbf{u}$ are the density and velocity of the fluid element, respectively.

- Momentum equation: This relates the rate of change of the fluid velocity to the forces acting on it,

$$\frac{\partial \mathbf{u}}{\partial t} + \mathbf{u} \cdot \nabla \mathbf{u} = -\frac{1}{\rho} \nabla p, \tag{3.1.2}$$

  where $p$ is the fluid pressure. Notice that the expression $\mathbf{u} \cdot \nabla \mathbf{u}$ is an advective term due to the gas parcel is moving with velocity $\mathbf{u}$.

As we will simulate dense structures, which are nearly isothermal, we do not need to solve the energy conservation equation. This is a good approximation as the radiative cooling finds equilibrium with the heating processes in densities greater than $10^2$ cm$^{-3}$, so they approach to a nearly isothermal behavior (Myers (1978),

Wolfire et al. (1995)). Different methods have been developed in order to approximate a solution for this set of equations. In this work we use a mesh-based method to discretize the space into a finite number of cells or elements assigning them dynamic and thermodynamic properties to evolve the system (Girault & Raviart, 2012).

## 3.2 FLASH Code

For our numerical models, we use the Eurelian adaptive mesh refinement (`AMR`) FLASH v4.3 code (Fryxell et al., 2000b; Dubey et al., 2009). [1] In order to integrate the hydrodynamic equations, we use a finite-volume method, referred as MUSCL-Hancock Scheme (Waagan, 2009). For the evolution and analysis of the model, two modules were the mostly used and are described in the following sections.

### 3.2.1 Self-gravity module

To compute the gravitational forces between the cells within the simulation, it is needed an efficient numerical method to solve the gravitational Poisson equation,

$$\nabla^2\phi(r) = 4\pi G\rho(r). \tag{3.2.1}$$

Once we determine the gravitational potential ($\phi$) the gravitational acceleration ($\vec{a}$) is then obtained by differentiating the potential, i.e., $\vec{a} = -\nabla\phi$.

We use the Tree based solver algorithm for the self-gravity presented in Wünsch et al. (2018), which is mostly based on the Barnes & Hut (1986) method for N-body simulations (Salmon & Warren, 1994; Springel, 2005). While others schemes scales as $N^2$ (where $N$ corresponds to the resolution elements) using a direct summation, a Tree based solver scales with $N \log N$, making it more efficient maintaining good precision (Clark et al., 2011).

This method consists of a global octal tree organized in nodes (or branches), in which the whole computational box is the root node and the individual cells are the leaves. A *tree walk* is done and only the tree nodes are needed for the calculation of the potential. There are four main parts in the algorithm of the tree solver:

[1] `https://flash.rochester.edu/site/index.shtml`

**1**.- Communication of block properties. It consists in exchanging information about the properties of each block between processors, such as the position, size, and level of refinement. This part is only needed if the AMR grid changes.

**2**.- Building the tree. This part involves constructing a hierarchical octree structure over the entire computational domain, starting from the top-level AMR grid down to individual cells. This is done by recursively dividing each block into eight child blocks until a minimum block size is reached.

**3**.- Communication of the tree. The next step is to distribute the tree across multiple processors and ensuring that each processor has access to the part of the tree that it needs for calculations.

**4**.- Tree walk. Finally, each node is evaluated in the tree to determine whether it should be used for calculations or if its children should be opened for further evaluation (below we describe this criterion). This process is performed for each grid cell, and the result is a list of active nodes that contribute to the solution. The contributions of all active nodes are then integrated during the tree walk to obtain the final solution.

The criterion to determine if a given node is opened to consider their subnodes for the calculation of the potential is through the *opening angle* $\theta_{\rm tol}$ ($\theta_{\rm tol} \sim 0.5$ rad is enough to generate errors $\leq 1\%$; Clark et al., 2011).

To walk the tree, the nodes are opened, and the algorithm checks the angle $\theta$ subtended by the children nodes from the cell of interest; if $\theta < \theta_{\rm tol}$ the measurement is made using the child node properties (mass, position and center of mass), but if $\theta > \theta_{\rm tol}$, then the child node opened and the process is repeated until a new angle smaller than the *opening angle* appears.

### 3.2.2 Sink particle module

The FLASH code is an adaptive mesh refinement (AMR) code, which means that it can dynamically refine the mesh in regions of interest. This is done according to the Jeans criterion, which prevents artificial fragmentation by ensuring that the local Jeans length ($\lambda_J$) is well resolved with at least $n_J$ grid cells (usually $n_J = 4$ is enough

to prevent spurious fragmentation in simulations without magnetic fields; Truelove et al., 1997). Once we reach the maximum refinement level allowed, we can create a sink particle in cells that reach the critical density defined as

$$\rho_{\rm sink} = \frac{\pi c_s^2}{G\lambda_J^2} = \frac{\pi c_s^2}{G(n_J \Delta x)^2}, \tag{3.2.2}$$

where $c_s$ corresponds to the sound speed in the gas, and $\Delta x$ is the size of the smallest cell on the grid. For the purpose of this work, we will refer to the critical density in cm$^{-3}$ units, applying the conversion $n_{\rm sink} = \frac{\rho_{\rm sink}}{\mu m_H}$, where $\mu$ is the mean molecular weight and $m_H$ the hydrogen molecule mass.

However, this is just the first step for a sink particle to be created, after which we define a control sphere (of radius $r_{\rm acc} = 2.5 \times \Delta x$) around the cell and a series of checks must be completed (Federrath et al., 2010):

**1**.- The control volume must be in the highest level of refinement $l_{\rm max}$. This is necessary because sink particles require a high level of resolution in order to accurately capture the details of the gas dynamics in the vicinity of the sink particle.

**2**.- The gas in the control volume is converging towards the center of the cell, where the sink particle will be placed. The code computes the divergence of the flow velocity within the control volume to determine if the flow is converging or diverging.[2]

**3**.- There is a local gravitational potential minimum in the cell of interest.

**4**.- The gas in the control volume must be Jeans-unstable. This means that the gas is undergoing gravitational collapse and is likely to form a protostar, according to the Jeans criterion (see Section 2.1.1):

$$|W| > 2U, \tag{3.2.3}$$

where $W$ is the gravitational energy and $U$ is the internal energy.

[2]A negative divergence indicates that the flow is converging, while a positive divergence indicates that the flow is diverging.

**5**.- The gas in the control volume is gravitationally bound, so that:

$$W + U + K + \mathcal{M} < 0, \tag{3.2.4}$$

where $K$ is the kinetic energy and $\mathcal{M}$ is the magnetic energy. If equation 3.2.4 holds, then is safe to say that the gas will not be dispersed by other forces, such as magnetic fields or pressure gradients.

**6**.- The *Proximity Check*, a new sink particle can not be created within the accretion radius $r_{\rm acc}$ of another sink particle.

If a cell successfully passes all the previous conditions, then a sink particle is placed at its center. If the *Proximity Check* fails, instead of creating a sink particle, we check if the existing sink can accrete the overdensity of the cell.

If a cell with coordinates $\{i, j, k\}$ within $r_{\rm acc}$ has its gas density above $\rho_{\rm sink}$, a mass increment parameter $\Delta M$ is computed as,

$$\Delta M = \left[\rho_{\{i,j,k\}} - \rho_{\rm sink}\right] \Delta V_{\{i,j,k\}}. \tag{3.2.5}$$

To determine if this mass increment can be accreted by the sink, the following checks must be satisfied:

- In case $\Delta M$ is within the $r_{\rm acc}$ of multiple sink particles, we measured the gravitational binding of $\Delta M$ for each of the sinks and select the one with the strongest bound to be the one accreting the gas.
- The kinetic energy of $\Delta M$ is measured and compared to its gravitational binding energy, so we can check if $\Delta M$ is moving toward the sink (i.e. negative radial velocity).
- If the position of $\Delta M$ is within the single central cell in which the sink particle is located, then the accretion is made without any checks, so numerical issues can be avoided.

Having completed these tests, the gas is accreted by the sink, conserving mass, linear and angular momentum, magnetic flux, etc., and the particle is moved towards the center of mass of the sink-gas system defined prior to the accretion.

## 3.3 Numerical model of an idealized gravitational collapse

In order to understand the basic concepts for the differential collapse of a dense core, an idealized model is constructed in this work. It consists of a numerical box of size $L_x = L_y = L_z = L_{\rm box} = 4$ pc, containing cold molecular gas ($\mu = 2.3$) with a background uniform density $\rho_0$. We place a gaussian overdensity at the center of the numerical box, so the mass density of a given cell with a position $\{i, j, k\}$ is given by

$$\rho_{n,\{i,j,k\}} = \rho_0 + \rho_0 e^{-\frac{(r_{\{i,j,k\}} - r_0)^2}{2\sigma^2}}, \tag{3.3.1}$$

where $r_{\{i,j,k\}}$ is the position of the cell, $r_0$ the position of the center, and $\sigma$ is the width of the gaussian profile, selected to be in direct relation with the size of the numerical box, $\sigma = L_{\rm box}/5$.

Our simulations are isothermal, with $T_0 = 10$ K (resulting in $c_s = 0.189$ km/s), which is reasonable for dense molecular cores (Ferrière (2001), Table 1.1). A detailed explanation regarding the main parameters to study and a table characterizing our numerical experiments are presented in the following sections of this chapter. Note that our initial conditions are similar to those used in Naranjo-Romero et al. (2015).

### 3.3.1 Boundary Conditions

In FLASH, the conditions at the boundaries are established in virtual areas called *guardcells* or *ghostcells* located outside the physical domain. To enable code refinement and parallelization, the computational domain is divided into several subdomains or blocks. Each block is surrounded by a perimeter of *guardcells* that contain information from neighboring blocks. If the block is at the boundary of the physical domain, the *guardcells* are filled with the appropriate boundary conditions (BCs; Fryxell et al., 2000a).

In this work, two types of BCs are selected: *Open* and *Closed* boundaries.

In FLASH, the first boundary selected is the *outflow* type. This forces a zero-gradient boundary, hence setting the values of the fluid variables (e.g., density, velocity, and pressure) in those boundaries at the same value as the corresponding closest

cell within the domain. This BC type allows shocks to leave the computational box and, in contracting systems, inject material (inflow) to prevent empty cells at the boundaries.

The other BC selected is the *diode* type. It is similar to the *outflow* type, except that it does not allow the gas flow into the domain. If necessary, the normal velocity components in guard cells are set to zero (Ferziger & Peric, 2001).

For the purpose of this work, the outflow type BC (hereafter OBC, for Open BCs) is chosen because it mimics a situation when the system in collapse always has a mass inflow, and the system is considered not-isolated.

On the other hand, the diode BC type (hereafter CBC, for Closed BCs) is chosen because it will not allow any material to flow into the system. This is equivalent to an isolated collapse, and the system has a fixed material reservoir to accrete onto the core and sink.

In the next subsection, we describe the combination of boundary conditions (BCs) used in our simulations. The specific BCs used are shown in Table 3.1.

### 3.3.2 Simulation parameters

Four simulations were performed by varying the BCs (as explained in the previous section) and the values of the initial uniform number density $n_0$,. For this, we select $n_0$ to be 82.46 cm$^{-3}$ and 824.65 cm$^{-3}$, so the mean number density at the start of the simulation $\langle n \rangle$, including the gaussian overdensity at the center of the numerical box, will be approximately 100 cm$^{-3}$ and 1000 cm$^{-3}$, respectively. Note that the Gaussian overdensity (Equation 3.3.1) represents the seed of the collapse. As the collapse proceeds, number densities greater than $10^5$ cm$^{-3}$ appear, along with strong density gradients, on sub-parsec scales. This allows us to study the properties of dense cores and compare them to their observational counterparts (see Table 1.2).

Table 3.1 shows important parameters from each of the numerical experiments. In general, the values presented in the table can be divided in three blocks:

- The first three rows are the values related to the mean initial number density ($\langle n \rangle$), being $\langle \tau_{ff} \rangle$ the gravitational free-fall time (see Section 2.2.1), which was calculated as

$$\langle \tau_{ff} \rangle = \sqrt{\frac{3\pi}{32G(\langle n \rangle \mu m_H)}}. \tag{3.3.2}$$

- The next four rows correspond to the resolution parameters and the sinks particle module (see Section 3.2.2). It is important to recall that since the critical density $n_{\rm sink}$ depends on the maximum refinement level possible $l_{\rm max}$, and this has to be integers numbers, there is not enough freedom to change $n_{\rm sink}$ to a specific desired value. The selection of $n_{\rm sink}$ was made so the ratio between $n_{\rm sink}$ and $n_0$ would be the most similar possible between the four simulations[3]. The parameters $\Delta x$ and $r_{\rm acc}$ corresponds to the minimum cell size and the accretion radius of the sink, respectively. The $r_{\rm acc}$ was calculated as shown in Section 3.2.2, and $\Delta x$ is obtained as

$$\Delta x = \frac{L_{\rm box}}{2^{l_{\rm max}+2}}. \tag{3.3.3}$$

- The last row shows the boundary condition selected for each simulation, with *Closed* referring to Diode type BC, and *Open* to Outflow type BC. See section 3.3.1 for a more detailed explanation on each BC.

### 3.3.3 Core Definition

As part of the analysis made for each simulation, a set of density thresholds were selected to define the *core* and explore how this definition affects its accretion and star formation activity.

This is implemented by selecting any cell whose density is greater than the density threshold $n_{\rm thr}$. Then, all the identified cells will create a group defined as the *core*, and their volume and mass will be used for calculations such as core mass ($M_{\rm core}$), core density ($\rho_{\rm core}$), core accretion ($\dot{M}_{\rm core}$), and other related values.

The chosen density thresholds are: $n_{\rm thr} = 10^3$ cm$^{-3}$ to represent a low density clump, $n_{\rm thr} = 10^4$ cm$^{-3}$ to represent a transition step between a clump and a core,

[3]Note that the values obtained are consistent with the density range observed in star forming regions (André et al., 2014, and see Table 1.2)

| Parameters | Simulations | | | |
|---|---|---|---|---|
| | C100 | O100 | C1000 | O1000 |
| $n_0$ [cm$^{-3}$] * | 82.46 | | 824.65 | |
| $\langle n \rangle$ [cm$^{-3}$] | 100 | | 1000 | |
| $\langle \tau_{ff} \rangle$ [Myr] | 3.38859 | | 1.07157 | |
| $l_{\max}$ * | 6 | | 8 | |
| $\Delta x$ [pc] | 0.016 | | 0.0039 | |
| $r_{\rm acc}$ [pc] | 0.039 | | 0.0098 | |
| $n_{\rm sink}$ [cm$^{-3}$] | $4.715\times10^4$ | | $7.544\times10^6$ | |
| Boundary * Type | Closed | Open | Closed | Open |

* Input Parameters.

Table 3.1: Parameters from the four simulations performed in this work. The columns correspond to specific simulations, and within each row, different important parameters are presented for the characterization of every simulation. In order, $n_0$ corresponds to the initial uniform density, $\langle n \rangle$ is the initial mean density, $\langle \tau_{ff} \rangle$ is the gravitational free-fall time (Equation 3.3.2), $l_{\max}$ is the highest refinement level possible in the simulation, $\Delta x$ is the minimum cell size in the box, $r_{\rm acc}$ is the accretion radius of the sink particle, $n_{\rm sink}$ is the critical density for a sink to be formed, and the *Boundary Type* row tells the chosen BC.

and $n_{\rm thr} = 10^5$ cm$^{-3}$ to represent a high density core. Also, we chose another density threshold to carry out an intermediate analysis in some cases: $n_{\rm thr} = 4 \times 10^4$ cm$^{-3}$.

The criterion we use to define our structures can be justified by observations: different species of molecular gas emit from different regions, depending on the density and temperature required for them to become collisionally excited and emit radiation (e.g., Williams et al., 2000).

For example, the most common low density tracer for clumps is the $^{13}$CO molecule, which is abundant in regions with high density molecular gas. On the other hand, a useful high density tracer to identify dense cores is the low-level transitions of $NH_3$ and $N_2H^+$, because they remain detectable at densities were usually other molecules would have heavily depleted (e.g., Pillai et al., 2006, see Section 1.2.1).

# Chapter 4

# Results

A total of four simulations were performed in this work (see Section 3.3.2 for the initial conditions of each one). In general, all of them are gravitationally unstable and shows the expected behavior of a spherical local collapse (see Chapter 2, and the right panel of Figure 2.1), with the mass flowing towards the center of the numerical box and collapsing from the outside-in, one sink particle appears eventually at the center of the core during the time interval of study. From now on, we will refer to the O100 and C100 models as the low-mass or low-density models/cores, and the O1000 and C1000 models as the high-mass or high-density models/cores, with the $O$ referring to models with OBCs and the $C$ to models with CBCs.

## 4.1 General evolution

Two snapshots of each simulation are presented in Figures 4.1 and 4.2. These snapshots were selected to represent two different evolutionary stages. The first one (left panels of each figure) shows an early stage, where signatures of gravitational collapse can barely be appreciated ($t_1 = 2.2$ Myr for C100 and O100, and $t_1 = 748.7$ kyr for C1000 and O1000). The second one corresponds to the time when the sink particle appears ($t_2 = 3.1$ Myr for C100 and O100, and $t_2 = 867.4$ kyr for C1000 and O1000). In terms of the free-fall time, the times mentioned above for C100 and O100 corresponds to $t_1 = 0.65\tau_{ff}$ and $t_2 = 0.92\tau_{ff}$, where $\tau_{ff} = 3.39$ Myr is the free-fall time at the beginning of the simulation. On the other hand, the times mentioned for C1000 and O1000 correspond to $t_1 = 0.70\tau_{ff}$ and $t_2 = 0.81\tau_{ff}$, where $\tau_{ff} = 1.07$ Myr.

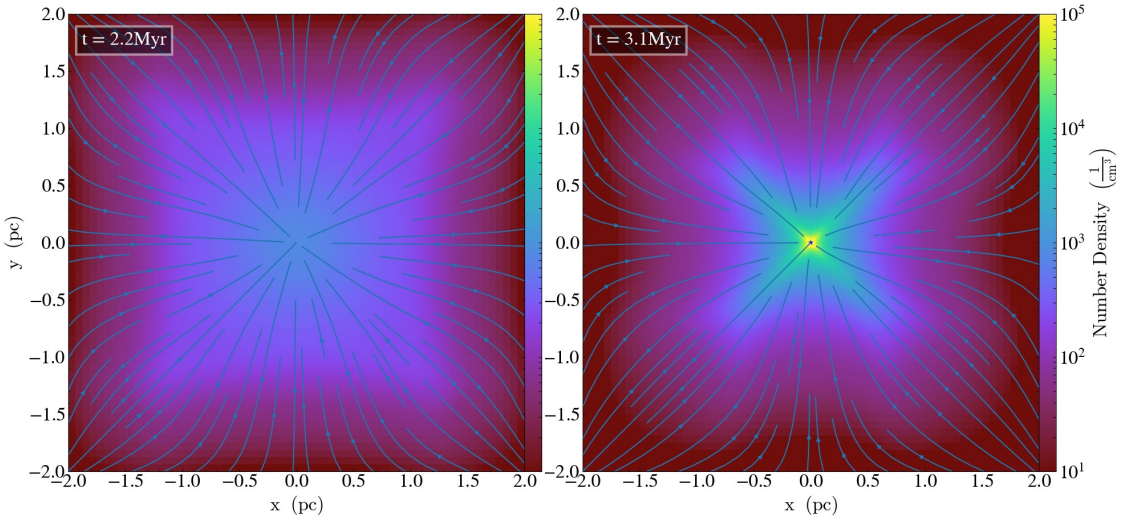


(a) C100 simulation.

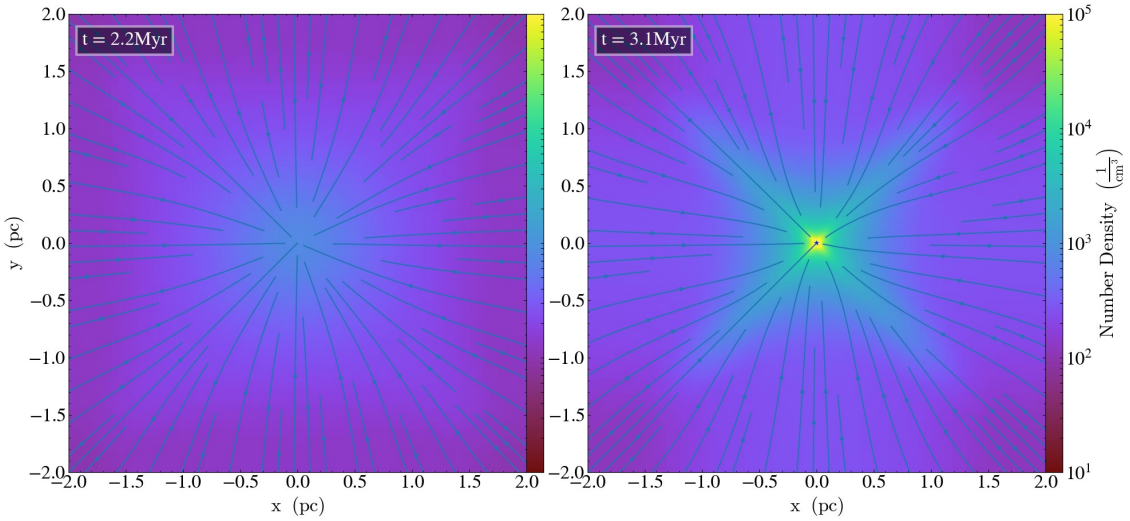


(b) O100 simulation

Figure 4.1: Number density slices for the simulations with $\langle n \rangle \approx 100$ cm$^{-3}$ in two stages of their evolution. The top panels represent the simulation labeled as C100, while the bottom panels are for the O100 simulation. The left panel is an early stage of the evolution ($t = 2.2$ Myr $= 0.65\tau_{ff}$) and the right panel is the snapshot immediate after the creation of the sink ($t = 3.1$ Myr $= 0.92\tau_{ff}$). The blue streamlines show the inflow velocity of the gas.

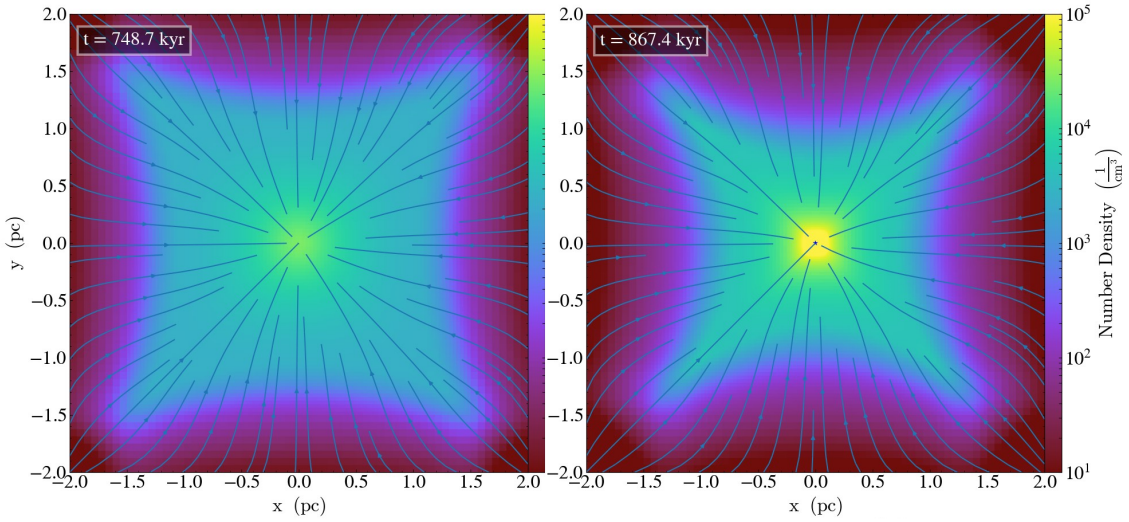


(a) C1000 simulation

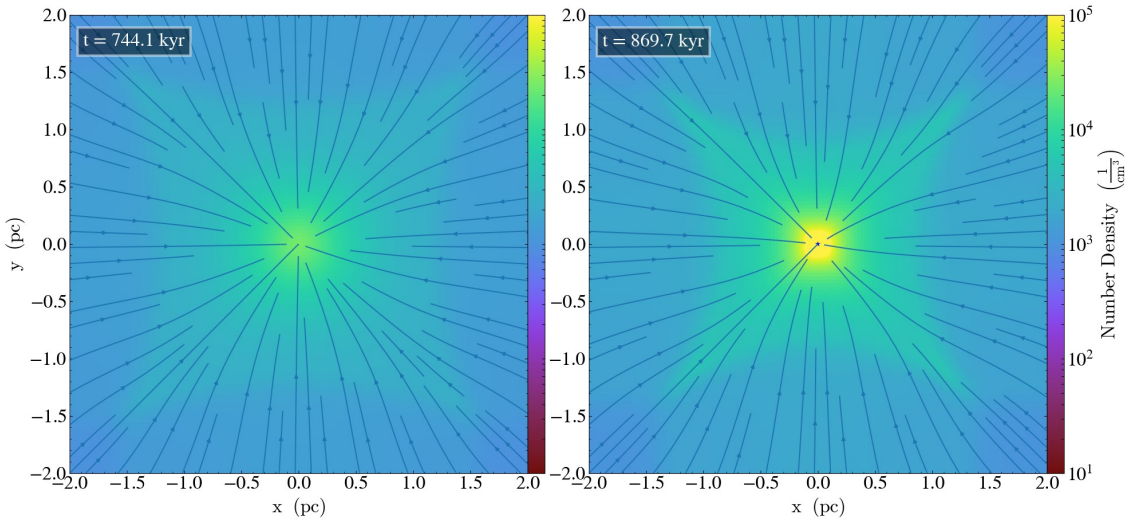


(b) O1000 simulation

Figure 4.2: Same as Figure 4.1, but for the simulations with $\langle n \rangle \approx 1000$ cm$^{-3}$.The top panels represent the simulation labeled as C1000, while the bottom panels are for the O1000 simulation. The left panel is an early stage of the evolution ($t = 748.7$ kyr $= 0.70\tau_{ff}$) and the right panel is the snapshot immediate after the creation of the sink ($t = 867.4$ Myr $= 0.81\tau_{ff}$). The blue streamlines show the inflow velocity of the gas.

As expected, the evolution time (the free-fall time; see Table 3.1) is shorter in our denser models. As seen in Figures 4.1 and 4.2, in the simulations with lower densities the sink is formed at $t_\star = 0.92\tau_{ff}$, and in the simulations with higher densities the sink is formed at $t_\star = 0.81\tau_{ff}$. Thus, the sink particle forms earlier in the models with higher density (C1000 and O1000). For each simulation, the formation time and the initial mass of the sink are shown in Table 4.1. Note that the initial mass of the sink is small (2-3 $M_\odot$), however it acquires most of its mass through mass accretion.

The fact that simulations with higher densities evolve *faster* than the others is because the thermal pressure is more important in the simulations with lower densities, so it provides more resistance (support) against the collapse.

## 4.2 Evolution of the density profiles

Figure 4.3 presents the evolution of the number density profiles for each simulation, showing the profiles for five times around the time (snapshot) when the sink is created (red line in each panel). Also, an $r^{-2}$ profile is plotted in the figure for reference, along with a dashed horizontal line representing the value of the threshold density for sink formation, $n_{\rm sink}$, for each simulation.

This figure shows a few interesting features. The density profiles get truncated in models with closed BCs in contrast with models with open BCs, in which the material is replenished from the faces of our cubic numerical box. Furthermore, the density profiles of all models exhibit a power-law behavior with a flat slope at early times. The slope then becomes steeper and saturates at a given value near the time of sink formation. From Figure 4.3 we compute the saturated slop (in the range of 0.1-1.0 pc) finding values of $1.72 \pm 0.008$, $1.67 \pm 0.013$, $1.70 \pm 0.01$, and $1.71 \pm 0.012$ for the C100, O100, C1000, O1000 models, respectively. Note that these values are consistent with the values reported in numerical models (e.g., Naranjo-Romero et al., 2015) and the overall evolution is consistent with the collapse model proposed by Gómez et al. (2021) (see Section 2.2.3).

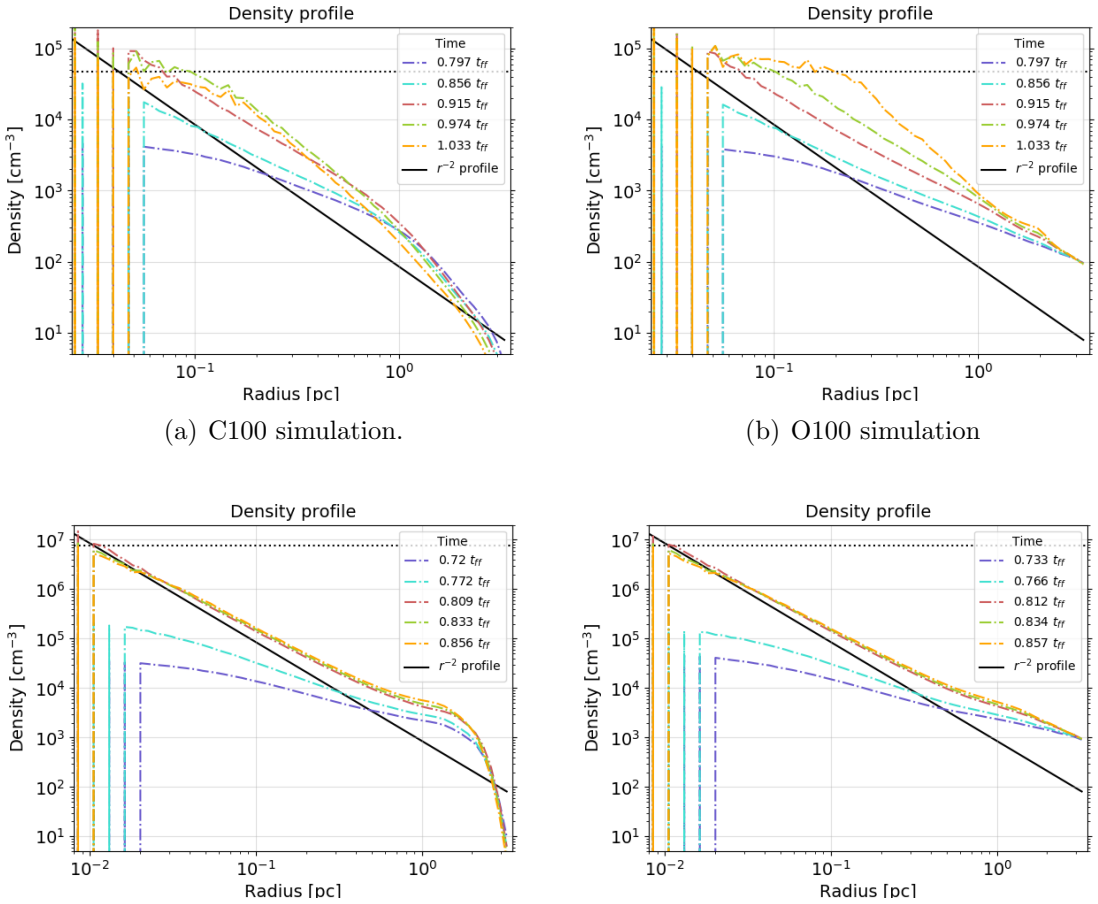


(a) C100 simulation. (b) O100 simulation

(c) C1000 simulation (d) O1000 simulation

Figure 4.3: Density profile for each simulation, showing five different times, the one immediately after the formation of the sink (red dot-dashed lines), and two before and two after that time. Also, each panel shows an $r^{-2}$ profile (solid black line), and a dashed horizontal line represents the threshold number density value for sink formation ($n_{\rm sink}$). The *top left panel* corresponds to the simulation labeled as C100, the *top right panel* to O100, the *bottom left panel* to the C1000, and the *bottom right panel* to the O1000.

| Initial Sink Values | Simulations | | | |
|---|---|---|---|---|
| | C100 | O100 | C1000 | O1000 |
| $t_0$ [Myr] | 3.0267 | 3.0207 | 0.8641 | 0.8631 |
| $t_0$ [$\tau_{ff}$] | 0.92 | 0.92 | 0.81 | 0.81 |
| $M_0$ [$M_\odot$] | 2.071 | 2.026 | 3.834 | 3.140 |

Table 4.1: Values of the time and sink mass ($t_0$ and $M_0$, respectively) computed in the snapshot when the sink first appears in each simulation.

## 4.3 The Star Formation Efficiency

As explained in Section 3.3.1, two different cases of boundary conditions (BCs) were chosen in order to study variations in the accretion from outside into the simulation box. Closed BCs (CBC) represent an isolated system where the material within the numerical box is the same along its evolution. Open BCs (OBC) represents a non-isolated system, so as it evolves, more material is being injected into the cubic numerical box.

In this section, we study the star formation efficiency (SFE), which is affected by mass accretion into the core and into the formed sink particle. In Figure 4.4 the accretion onto the sink particle ($\dot{M}_{\star,i}$) can be seen for each simulation, which is calculated as

$$\dot{M}_{\star,i} = \frac{M_{\star,i} - M_{\star,i-1}}{\Delta t}, \tag{4.3.1}$$

where $M_\star$ is the mass of the sink, the index $i$ denotes the step of the simulation where the measurement is being made, and $\Delta t$ is the time between the snapshots $i$ and $i-1$. The first thing to note is that in our high-mass cores (models O1000 and C1000) the sink accretes roughly at the same rate regardless of the chosen boundary conditions in contrast with the models O100 and C100, where the mass accretion into the sink depends crucially on the chosen BCs (see Figure 4.4). The difference in the accretion rates may be due to the fact that the low-mass cores (models O100 and C100) evolve further in the collapse, allowing the sink to accrete more of the available mass in the core.

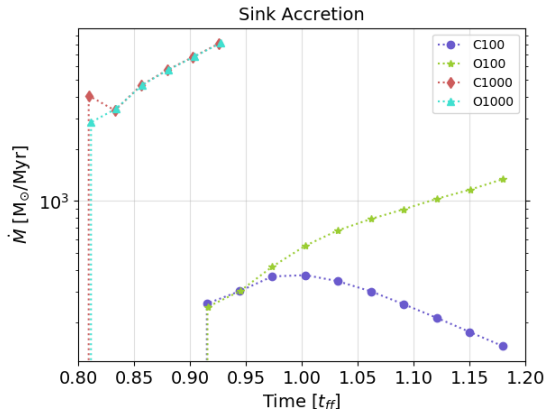


Figure 4.4: Evolution of the mass accretion into the sink (Equation 4.3.1) for each simulation.

Interestingly, in our low-mass models, the sink reaches 300 $M_\odot$ (which is the initial mass of the box) at $t = 1.29\tau_{ff}$ in the C100 model, and at $t = 1.08\tau_{ff}$ in the O100 model (see, e.g., green lines in Figure 4.5).

On the other hand, the core mass evolution depends on the core definition. Figures 4.5, 4.6, 4.7 and 4.8 show the evolution of the core, sink, and total mass in each of the four simulations, along with the instantaneous SFE (Equation 1.3.1), when the core is defined by threshold densities $n_{\rm thr} = 10^3, 10^4, 4\times10^4$, and $10^5$ cm$^{-3}$, respectively (the difference between the four figures is the density threshold for the core definition). The core mass evolution and the resulting SFEs can be summarized as follows:

- In general, the O1000 and C1000 models form more massive cores than the C100 and C100 models, regardless of the density threshold used to define a core. Therefore, the SFE is lower in the former models, which is expected according to Eq. 1.3.1 as the core mass ($M_{\rm core}$) is in the denominator of the expression.

- For cores defined with the lower density threshold ($n_{\rm thr} = 10^3\,{\rm cm}^{-3}$; Figure 4.5), the core mass is decreasing/increasing in time for the models with closed/open BCs. The sink mass evolves similarly, regardless of the BCs. This leads a lower SFEs in models with open BCs.

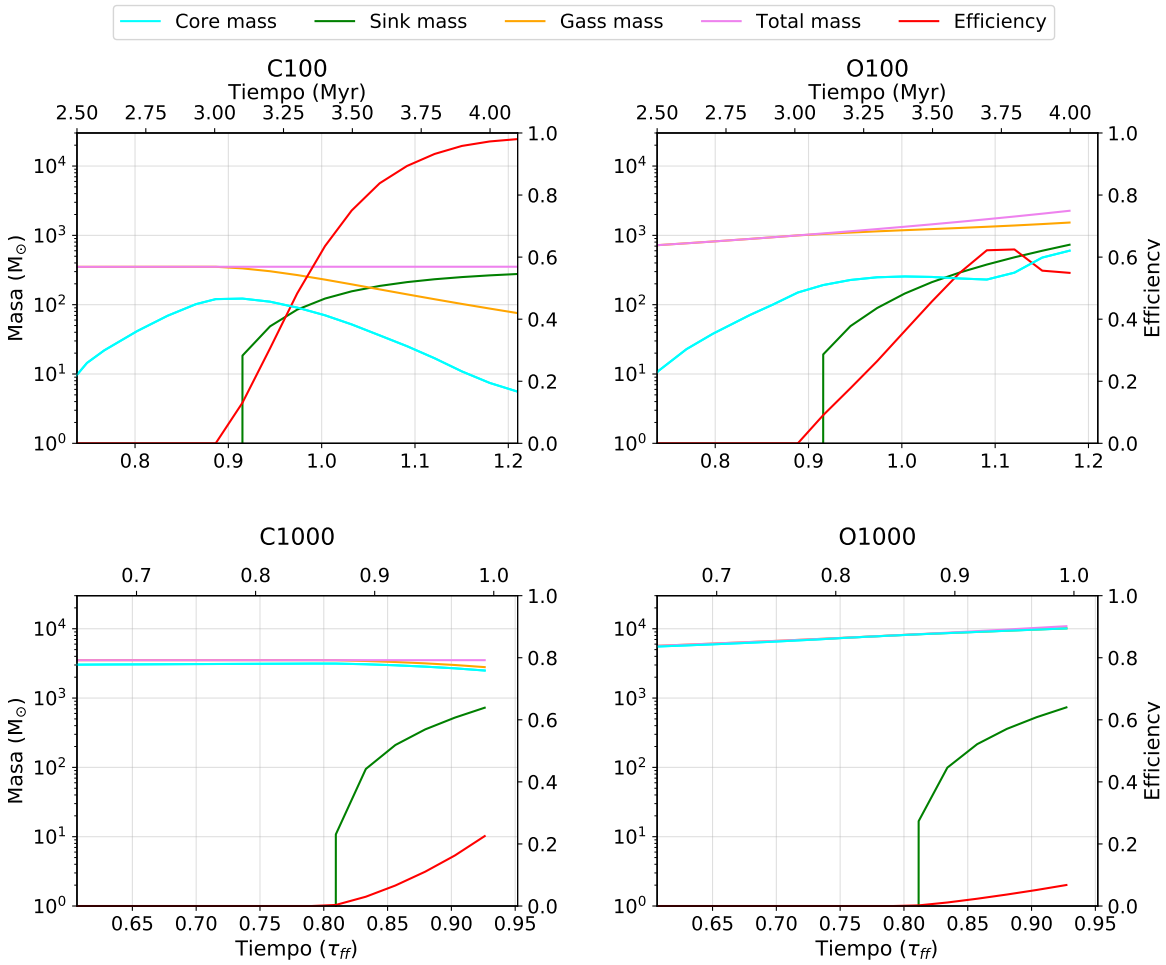


Figure 4.5: Mass and SFE (or Efficiency) evolution (left and right vertical labels, respectively) for each simulation. Here, we define the core with $n_{\rm thr} = 10^3$ cm$^{-3}$. The *top left panel* corresponds to the simulation labeled as C100, the *top right panel* to O100, the *bottom left panel* to the C1000, and the *bottom right panel* to the O1000 model. Cyan, green, yellow, purple and red lines represent the core mass, sink mass, total gas mass, total mass of the system and the SFE (Efficiency), respectively. To better understand the evolution, both the time in Myr (top x-axis) and in $\tau_{ff}$ units (bottom x-axis) are shown.

- For the cores defined with the higher density threshold ($n_{\rm thr} = 10^5\,{\rm cm}^{-3}$; Figure 4.8), the sink mass dominates the system. The sink mass is similar in models with open or closed BCs, resulting in a similar star formation efficiency (SFE).

Overall, the SFE depends on both the BCs and the core definition. However, this dependence is less evident in cores defined with a high density threshold. Although the SFE approaches 1 in the low-mass cores (models C100 and O100), this is not realistic according to observations, as they show values of SFE $< 50\%$ Lada & Lada (2003). Therefore, these models should be interpreted with caution, and the analysis should be considered valid only for times when the SFE is less than 0.5 (for $t < t_{ff}$).

## 4.4 The Star Formation Efficiency per Free-Fall time ($\epsilon_{ff}$)

We now quantify the $\epsilon_{ff}$ (Equation 1.3.2) for all our models. For this we need the SFR ($\dot{M}_*$ in Equation 4.3.1), the mean free-fall time (Equation 3.3.2), and the core mass, which we measure using different thresholds number densities ($n_{\rm thr}$; see Figures 4.5 to 4.8). In this work we calculate the time evolution of $\epsilon_{ff}$ for a given $n_{\rm thr}$ and also its radial profile for a given time. Figure 4.9 shows the evolution of $\epsilon_{ff}$ for each simulation with different core definitions. To illustrate the evolution of the $\epsilon_{ff}$ profile, Figure 4.10 shows different times for each simulation, including the time of sink formation. The results for the $\epsilon_{ff}$, in the time range of realistic SFEs ($< 0.5$; see red lines of Figures 4.5 to 4.8), can be summarized as:

- Figure 4.9 shows that the $\epsilon_{ff}$ is nearly constant.
- We find similar values of the $\epsilon_{ff}$ in our models, regardless of the chosen BCs (although there is a slight difference in the core defined with the lower number density threshold, $n_{\rm thr} = 10^3$ cm$^{-3}$).
- As the cores are defined with higher $n_{\rm thr}$, the values of $\epsilon_{ff}$ are slightly higher.
- Interestingly, the $\epsilon_{ff}$ is higher in our low-mass cores (models O100 and C100). This is unexpected, as one might naively expect that $\epsilon_{ff}$ would be higher in more massive cores, where there is more gas available to form stars.

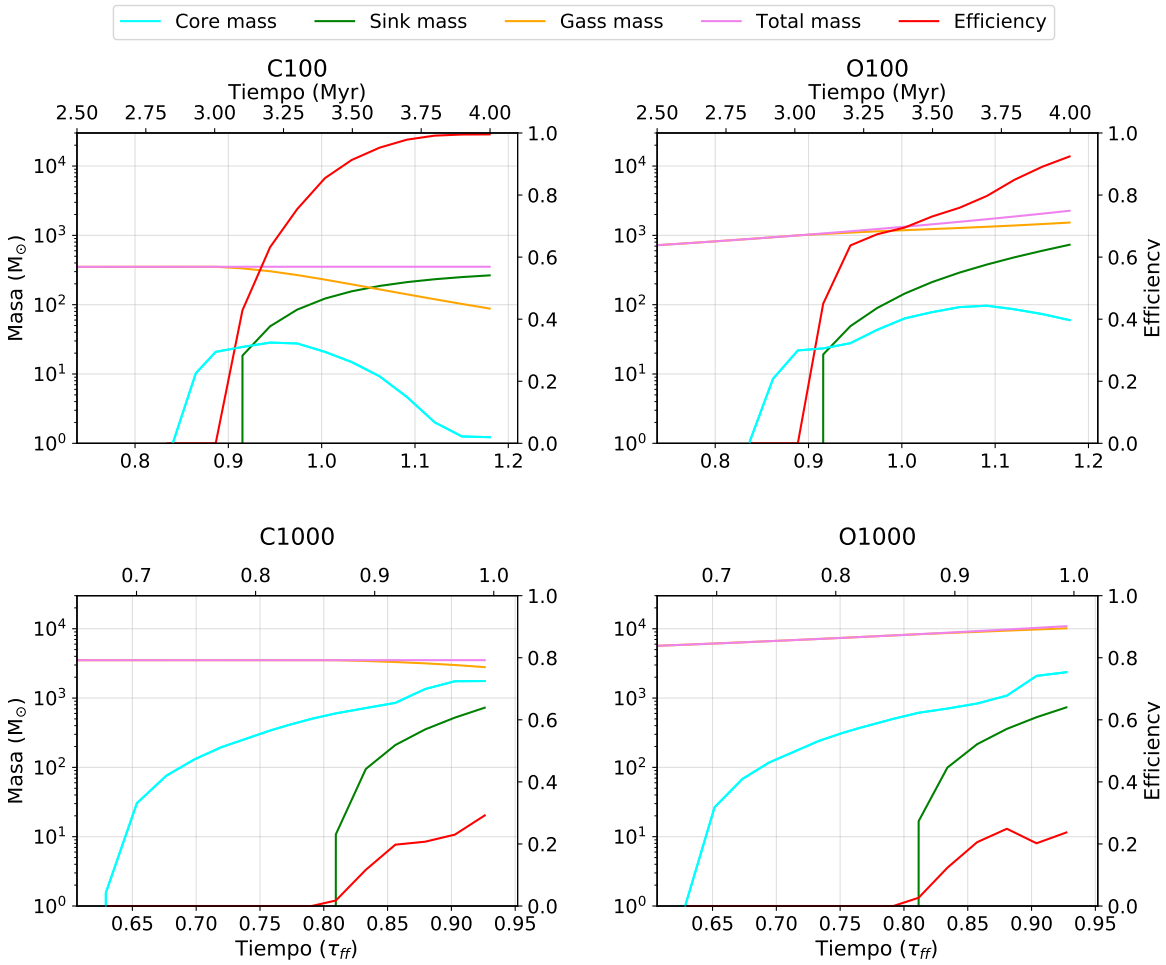


Figure 4.6: Mass and SFE (or Efficiency) evolution (left and right vertical labels, respectivelly) for each simulation. Here, we define the core with $n_{\rm thr} = 10^4$ cm$^{-3}$. The *top left panel* corresponds to the simulation labeled as C100, the *top right panel* to O100, the *bottom left panel* to the C1000, and the *bottom right panel* to the O1000 model. Cyan, green, yellow, purple and red lines represent the core mass, sink mass, total gas mass, total mass of the system and the SFE (Efficiency), respectivelly. To better understand the evolution, both the time in Myr (top x-axis) and in $\tau_{ff}$ units (bottom x-axis) are shown.

- The $\epsilon_{ff}$ profiles shown in Figure 4.10, are nearly constant in space (radius). Also, the curves for different times after the formation of the sink all have similar values of $\epsilon_{ff}$, implying that this parameter is nearly constant in time.

So our models exhibit a nearly constant $\epsilon_{ff}$ in time and space. In the next section, we provide a plausible explanation for the behavior of the $\epsilon_{ff}$ described here.

## 4.5 Discussion

In this section we discuss the previous results considering the general overview of the simulations and their evolution, and then the SFE and $\epsilon_{ff}$.

The results and measurements using the higher density thresholds to define the core must be taken carefully, since the core boundary could approach the sink accretion radius ($r_{\rm acc}$) and the core properties can be affected by the numerical implementation of the accretion process. In Figure 4.11 (see Section 4.5.1) we compare the core size ($r_{\rm core}$) with $r_{\rm acc}$ and we consider that the core properties we quantify are free of resolution issues when $r_{\rm core} > 4 \times r_{\rm acc}$. This figure tells us that practically all the cores are well-resolved (except for some points in the two smaller cores in C100 and O100) so we can discard numerical artifacts. This also tells us that the simulations with the higher initial densities are better resolved than the other two.

The first thing to note is that the identified density profiles saturate to values that are consistent with observations (see Figure 1.1). This suggests that most star-forming cores are dominated by self-gravity, as are our models. However, the slope of our density profiles saturates at $p \lessapprox 1.71$, which means that gravity alone cannot explain steeper slopes. Other physical ingredients, such as magnetic fields, must be taken into account.

Additionally, as $n_{\rm thr}$ increases, the SFE increases due to the cores being smaller and containing less mass. This effect is more noticeable in the C1000 and O1000 simulations because the sink mass grows more rapidly than the core mass (compare, for example, the green and cyan lines in Figure 4.8). This means that the sink mass is accreting matter at a faster rate than the core. Furthermore, when the density profile of the core reaches a power-law slope of 2 (i.e., $n_{\rm thr} \propto r^{-2}$), the core reaches a stationary state (Gómez et al., 2021). This means that the accretion rate is the same throughout the core, so all the mass that is accreted is transferred to the sink, maintaining the core mass roughly constant. This effect is more noticeable in our models with open boundary conditions (see, cyan lines in Figures 4.5 to 4.8).

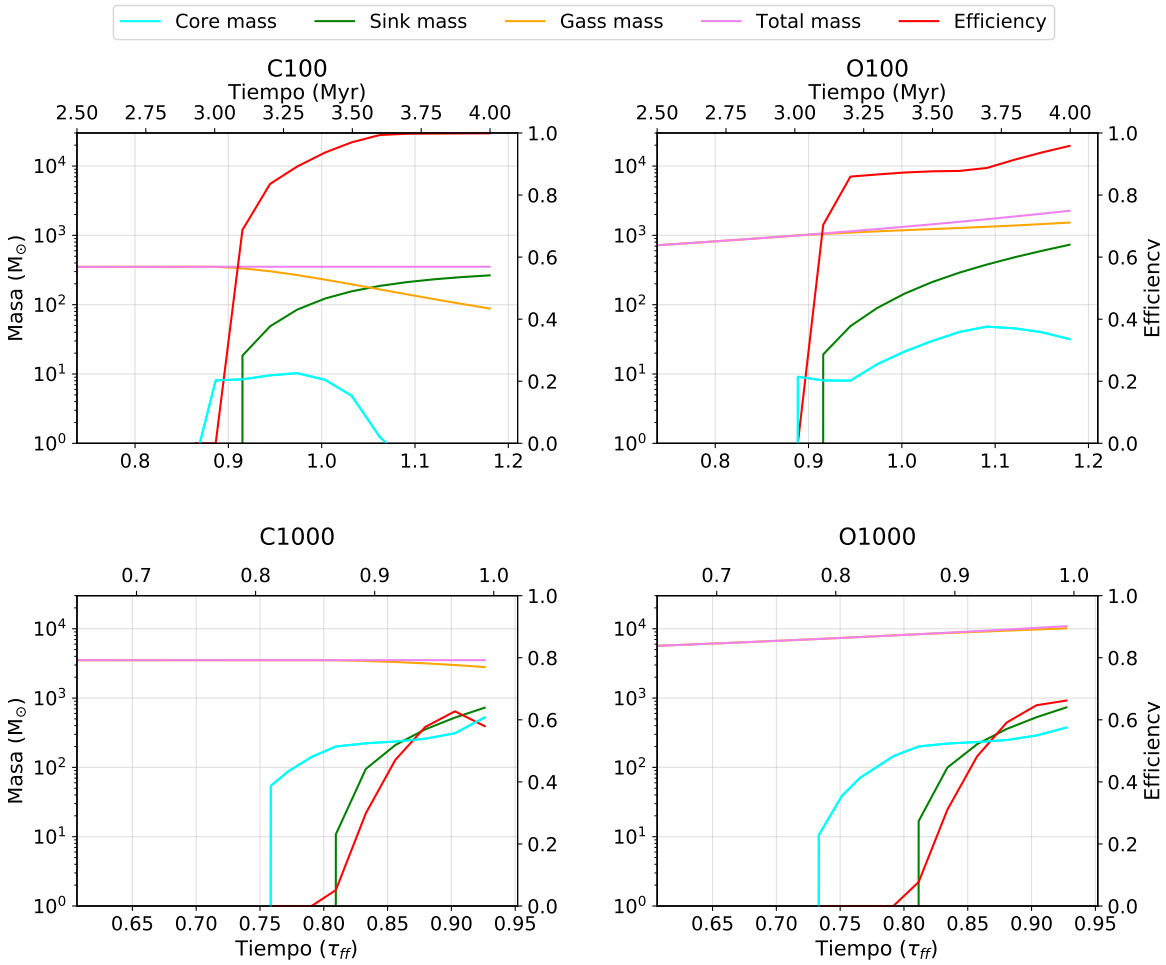


Figure 4.7: Mass and SFE (or Efficiency) evolution (left and right vertical labels, respectively) for each simulation. Here, we define the core with $n_{\rm thr} = 4 \times 10^4$ cm$^{-3}$. The *top left panel* corresponds to the simulation labeled as C100, the *top right panel* to O100, the *bottom left panel* to the C1000, and the *bottom right panel* to the O1000 model. Cyan, green, yellow, purple and red lines represent the core mass, sink mass, total gas mass, total mass of the system and the SFE (Efficiency), respectively. To better understand the evolution, both the time in Myr (top x-axis) and in $\tau_{ff}$ units (bottom x-axis) are shown.

On the other hand, Figure 4.4 shows how the accretion towards the sink in the C1000 and O1000 models have practically no variations between them, while in C100 the sink accretion is not as efficient as it is in O100. The difference between C100 and O100 happens because of the different BCs, as the open BCs allow the injection of

material in the numerical box, so the sink has an increasing reservoir of mass to accrete. However, the star formation efficiency (SFE) of these simulations grows rapidly, so its value is unrealistic after approximately one free-fall time. On the contrary, this difference in the sink accretion history is not observed between the C1000 and O1000 simulations because they evolve a lot quicker and have more gas available since the beginning, so they are less likely to be affected by the variations in the accretion (i.e. the boundary conditions).

Also, Figure 4.5 gives us some information about the difference in the SFE (Eq. 1.3.1) of the simulations. In general, the simulations with closed BCs have higher efficiencies than the ones with OBC (so the efficiency in C100 is higher than in O100, and in C1000 is higher than in O1000); this happens because the closed boundaries have less material available for the core to accrete, but the sink maintains an accretion rate similar between them (this effect can be more appreciable in the C100 and O100 simulations), causing the SFE of CBC models to approach 100%. However, this effect becomes less noticeable as we increase the number density threshold ($n_{\rm thr}$) used to define the core, as seen in Figures 4.5, 4.6, 4.7 and 4.8. These figures show the core and sink mass as well as the SFE for $n_{\rm thr} = 10^3$, $10^4$, $4 \times 10^4$, and $10^5$ cm$^{-3}$, respectively.

Regarding the SFE and $\epsilon_{ff}$, the first situation we notice in Figure 4.9 is the high values measured of $\epsilon_{ff}$, as the expected mean value for star-forming regions is $\epsilon_{ff} \approx 0.01$ within an order of magnitude (e.g., Krumholz et al., 2019), and we obtain values from 0.1 to even 100 in the smaller cores. This discrepancy could be explained with the following arguments:

- Resolved observations to date are at the scale of molecular clouds (e.g., Lada et al., 2010; Pokhrel et al., 2021), and there is not yet a direct measure of the efficiency in single cores that can be used as a reference. Note however that the values we found for the efficiency are consistent with the value reported by Louvet et al. (2014) for a mini-starburst ($\epsilon_{ff} \sim 0.1 - 1$).

- Our measurements of the efficiency come from the raw 3D data, whereas the observational determinations come from 2D column density maps, so we are not capturing the observational biases (Pokhrel et al., 2021).

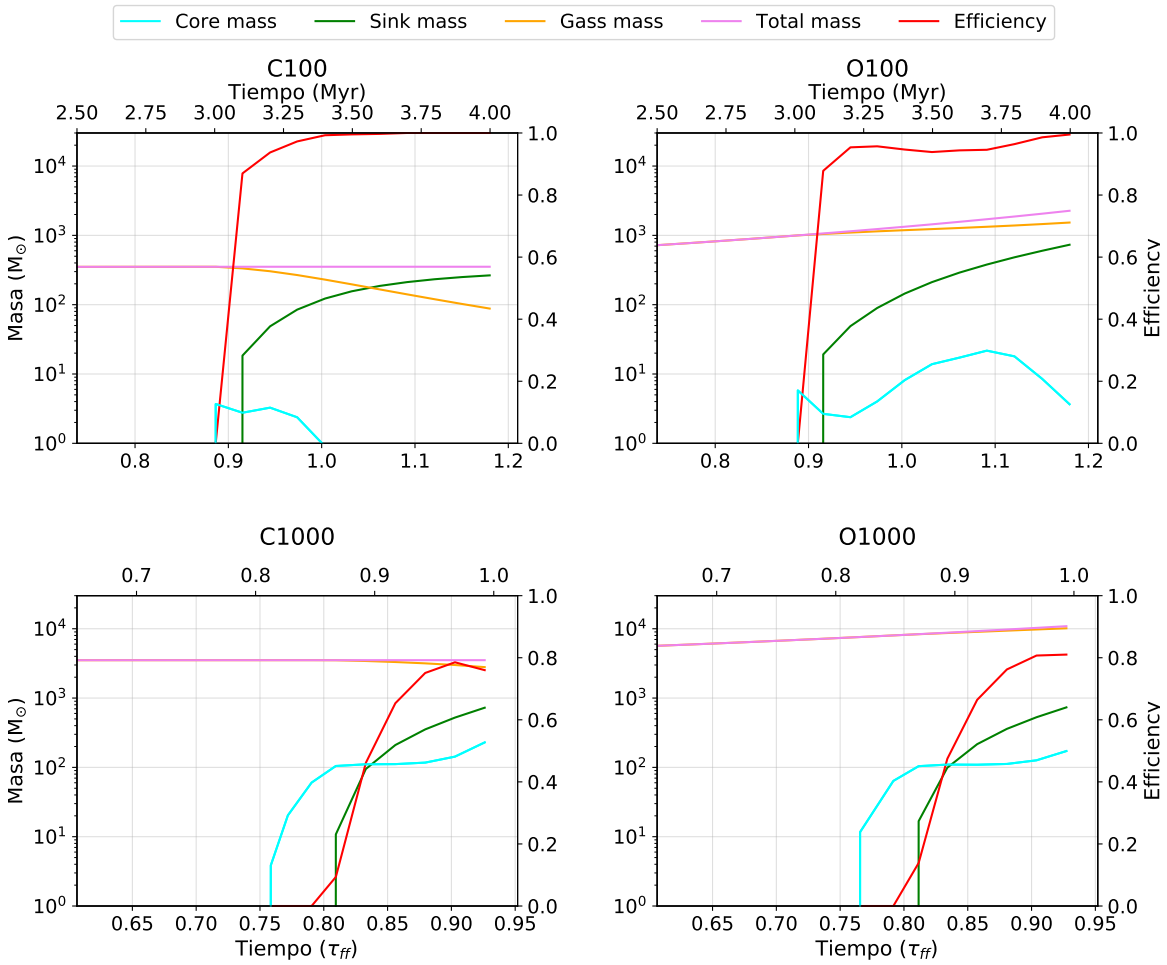


Figure 4.8: Mass and SFE (or Efficiency) evolution (left and right vertical labels, respectivelly) for each simulation. Here, we define the core with $n_{\rm thr} = 10^5$ cm$^{-3}$. The *top left panel* corresponds to the simulation labeled as C100, the *top right panel* to O100, the *bottom left panel* to the C1000, and the *bottom right panel* to the O1000 model. Cyan, green, yellow, purple and red lines represent the core mass, sink mass, total gas mass, total mass of the system and the SFE (Efficiency), respectively. To better understand the evolution, both the time in Myr (top x-axis) and in $\tau_{ff}$ units (bottom x-axis) are shown.

- We use the instantaneous star formation rate (SFR), which is increasing (accelerating) in time, whereas in observations the SFR is the average over some star formation timescale (e.g., Lada et al., 2010; Pokhrel et al., 2021), producing thus lower values of real SFRs, which increase on time (e.g., Stahler & Palla, 2005).

- This simulations have only one center of collapse, whereas observations show that cores contain several fragments or centers of collapse that compete to accrete mass (see, e,g., Palau et al., 2014).

- As the simulations do not have any stellar feedback nor magnetic fields or turbulence, there is no mechanism to stop or delay the accretion toward the core/sink, hence increasing the SFE, the SFR and $\epsilon_{ff}$. In this work we did not include these mechanism in order to understand the effect of self-gravity on the $\epsilon_{ff}$.

In Figure 4.9 we compare the evolution of $\epsilon_{ff}$ for our simulated cores defined with different threshold density, and we observe that $\epsilon_{ff}$ takes lower values for the lower density thresholds. Notice that the cores with lower density thresholds have more mass to accrete to the sink particle (as they are bigger in size they have more material available) but the sink accretion rate is the same regardless of the definition of the core. This effect happens due to $\epsilon_{ff}$ being calculated as the ratio between the accretion rate of the sink and the mass available (see Equation 1.3.2), then the more material is left within the core, the lower is the $\epsilon_{ff}$ measured.

This proves how the way we define the core can directly affect the efficiency measured within a region. This is important because in a star-forming region, the substructures are not isolated entities but part of a continuum, whose borders are arbitrarily defined either by observational or numerical biases.

We next study the spatial dependence of $\epsilon_{ff}$. We notice a similar behavior between the curve of the $\epsilon_{ff}$ evolution in the four cores, specially in the early times of their evolution. According to Figure 4.3, in these early times (i.e. the red curve, when the sink has just been formed), the curves have a tendency to $r^{-2}$ profiles, while the other curves are *attracted* by the $r^{-2}$ profiles, as predicted in the analysis by Gómez et al. (2021) (see Section 2.2.3). This scenario has important implications:

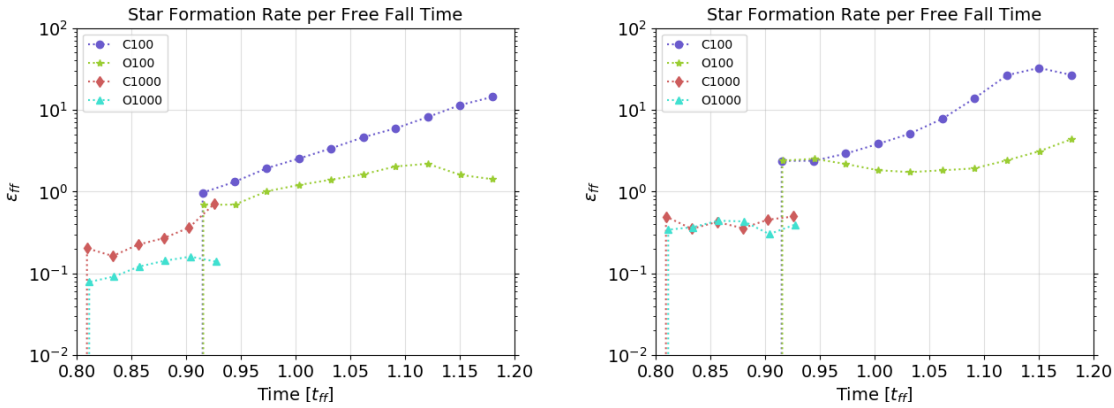


(a) $n_{\rm thr} = 10^3$ cm$^{-3}$




(b) $n_{\rm thr} = 10^4$ cm$^{-3}$

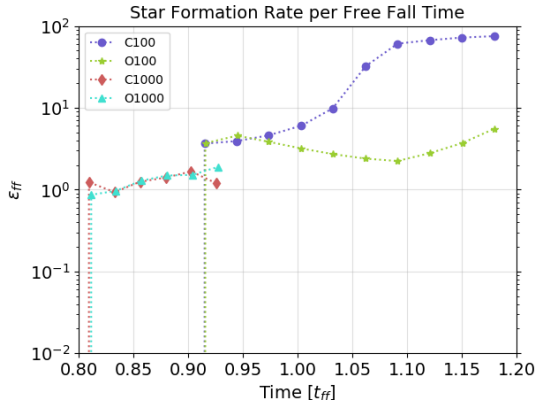


(c) $n_{\rm thr} = 4 \times 10^4$ cm$^{-3}$

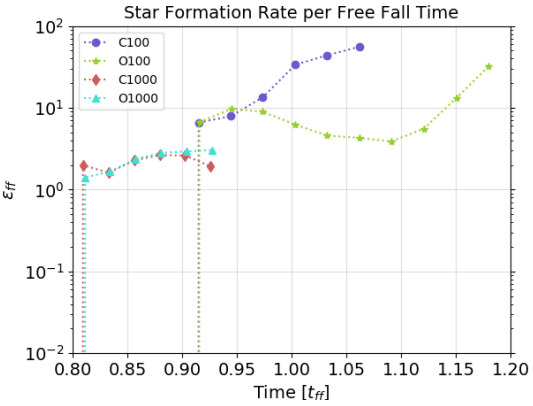


(d) $n_{\rm thr} = 10^5$ cm$^{-3}$

Figure 4.9: Evolution of the star formation rate per free-fall time ($\epsilon_{ff}$) for each simulation. In panel (a) the core is defined with the density threshold of $n_{\rm thr} = 10^3$ cm$^{-3}$, in panel (b) with $n_{\rm thr} = 10^4$ cm$^{-3}$, in panel (c) with $n_{\rm thr} = 4 \times 10^4$ cm$^{-3}$, and in panel (d) with $n_{\rm thr} = 10^5$ cm$^{-3}$.

- First, the $\tau_{ff}$ is proportional to $r$,

$$\rho \propto r^{-2} \quad \Rightarrow \quad \tau_{ff} \propto \rho^{-1/2} \propto r. \tag{4.5.1}$$

- We can approximate the mass by assuming a spherical core, thereby it presents the same proportionality to $r$,

$$M_{\rm core} = \frac{4\pi\rho r^3}{3} \quad \Rightarrow \quad M_{\rm core} \propto r. \tag{4.5.2}$$

- Finally, the sink accretion does not depend on the core radius, we notice that $\epsilon_{ff}$ must be $r-$independent, i.e.,

$$\epsilon_{ff} = \frac{\dot{M}_\star}{M_{\rm core}}\tau_{ff} \quad \Rightarrow \quad \epsilon_{ff} \text{ is } r - \text{independent.} \tag{4.5.3}$$

To illustrate this first order calculation, in Figure 4.10 the profiles of $\epsilon_{ff}$ are shown, in which we quantify $\tau_{ff}(r)$, $M_{\rm core}(r)$ and, finally, $\epsilon_{ff}(r)$. Here we can see the $r-$independent behavior in the curves for three different times, specially in the simulations with closed BCs, when the system is isolated, hence improving the *idealization* of the collapse.

The results in these plots can be compared with the observations shown in the right panel of Figure 1.2, as we present the *clouds* in different times of it their evolution and they maintain in similar $\epsilon_{ff}$, as well as the r-independent behavior mentioned earlier.

### 4.5.1 Resolution effects

We perform a sanity check to determine if our cores are well resolved. For this, we determine if the cores defined in our simulation are large enough to be resolved by the numerical grid. We do this by comparing the size of the cores to the accretion radius of the sink ($r_{\rm acc}$, for details about this parameter, see Section 3.2.2). The core size is calculated by taking the total density ($\rho_{\rm core}$) and mass ($M_{\rm core}$) of the core at the time measured, and approximating the core as a sphere, so

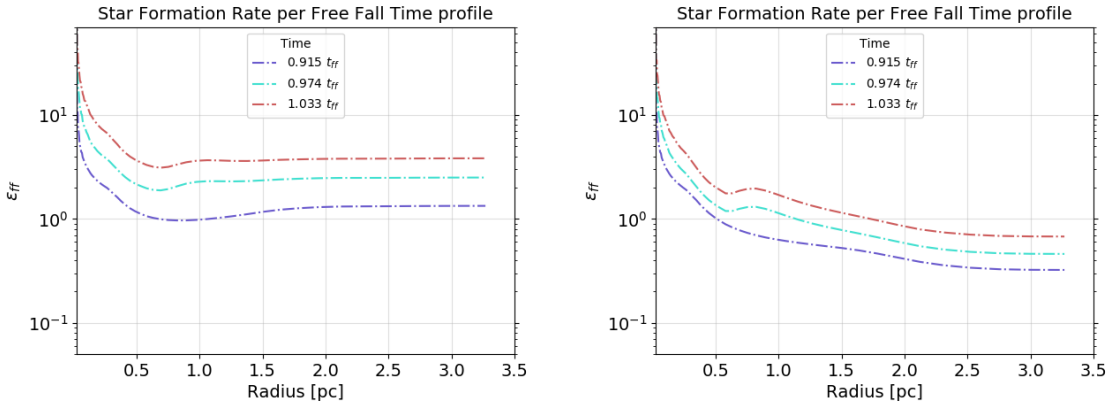


(a) C100 simulation (b) O100 simulation

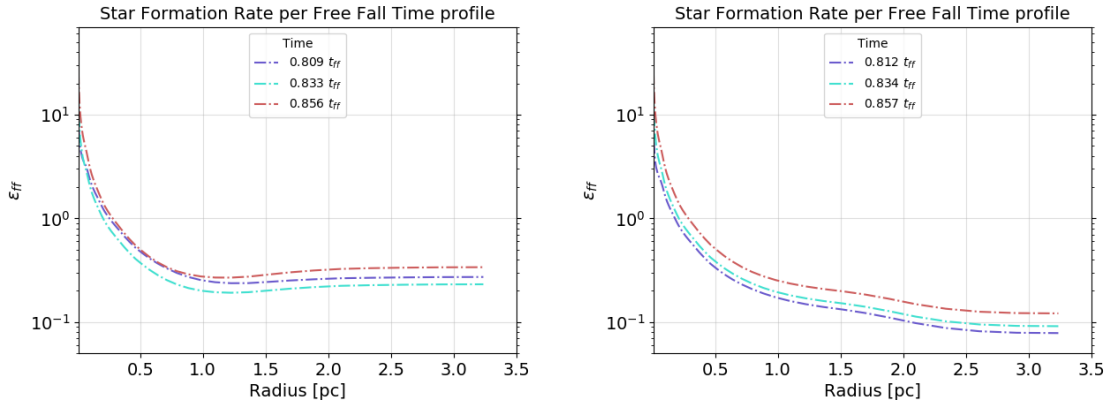


(c) C1000 simulation (d) O1000 simulation

Figure 4.10: Profiles of the star formation efficiency per free-fall time ($\epsilon_{ff}$) for each simulation. The *top left panel* corresponds to the simulation labeled as C100, the *top right panel* to O100, the *bottom left panel* to the C1000, and the *bottom right panel* to the O1000.

$$r_{\rm core} = \sqrt[3]{\frac{3M_{\rm core}}{4\pi\rho_{\rm core}}}. \tag{4.5.4}$$

Figure 4.11 shows the evolution of the ratio $r_{\rm acc}/r_{\rm core}$ for all our models and cores (defined at different threshold densities). Values of this ratio below the horizontal

line in this figure mean that the core is well resolved, i.e., $r_{\rm core} > 4 \times r_{\rm acc}$[1]. From this figure, we can see that all our cores are well resolved, except for the core defined with $n_{\rm thr} = 10^5$ cm$^{-3}$ in the C100 model and some points of a couple of other cores). So in general, our cores are well resolved and we can discard effects related with the numerical recipe of gas accretion onto the sink (see Section 3.2.2).

### 4.5.2 Limitations

The main issues faced in this work corresponds to the nature of the simulations. Because the simulations were not performed with spherical symmetry and the collapse occurs within a square box, a border effect can be appreciated that is not realistic, in the context of an idealized spherical gravitational collapse.

One example is the high density cross-like structures formed when the simulations have evolved some time, as can be barely seen in the right panels of each block in Figures 4.1 and 4.2, caused because of the geometry of the box. This effect can deviates slightly the core from the spherical geometry, and can can affect the measurements at late times. This numerical defect is more noticeable in simulations with OBCs at late times, because the constant injection of material onto the numerical box can lead to the accumulation of spurious density structures.

The final limitation in our work is the lack of other physical ingredients needed to simulate a more realistic core. For example, the magnetic field or the turbulence cause a delay in the evolution of the MC and the collapse can be delayed (Federrath & Klessen (2012), Hennebelle & Inutsuka (2019)). Also, the feedback from the star (radiative and mechanic) compete with the accretion to the point that can completely stop it, hence reducing significantly the measured SFEs (e.g., Dale, 2017).

Additionally, the dense cores are not isolated throughout the cloud, nor are they in the center of the collapsing MC, but they are inside filament structures (see Section 1.2.1) and present a hierarchical collapse (Vázquez-Semadeni et al., 2019), so the properties of a given core could be affected for other cores or the filament itself.

[1]The value of 4 was chosen to ensure that the total volume of the core would be much greater than the volume related to the accretion radius, while still allowing for smaller cores to be taken into account. Note that with a value of 4, the volume of the core would need to be 64 times greater than the volume related to the accretion radius.

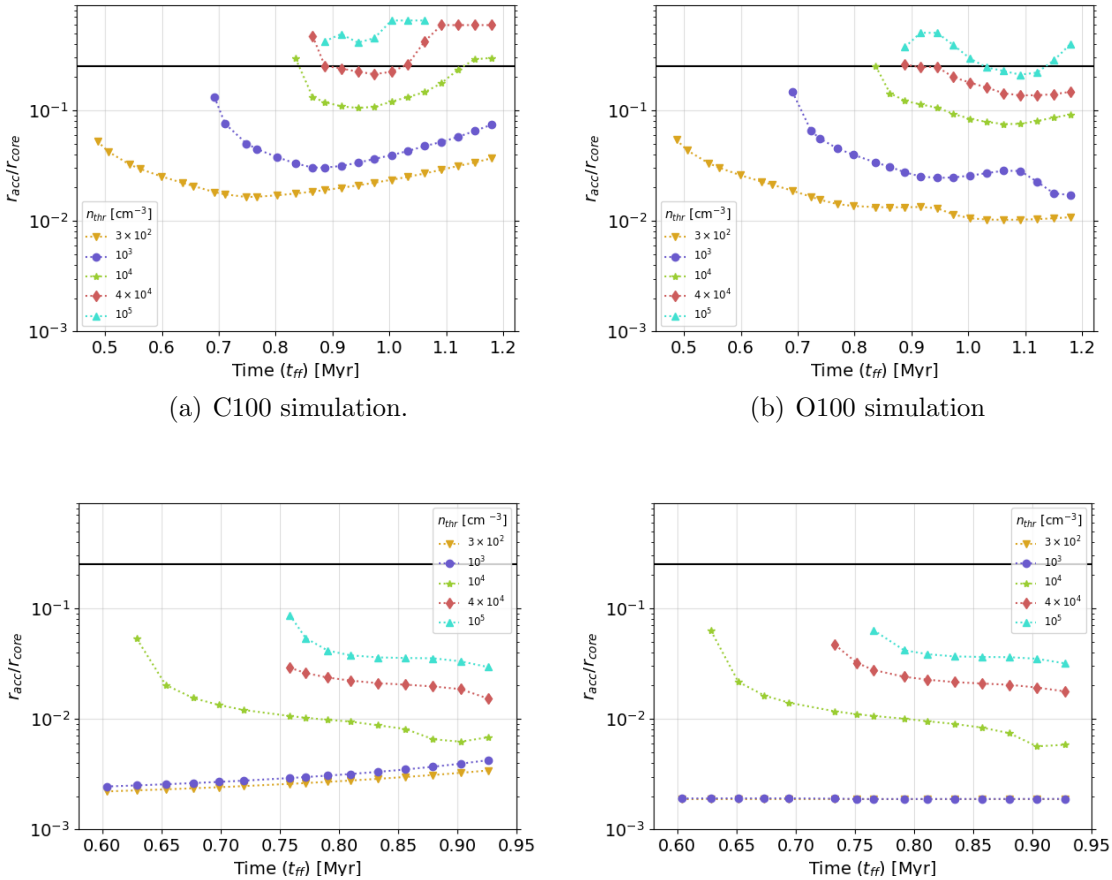


(a) C100 simulation.

(b) O100 simulation

(c) C1000 simulation

(d) O1000 simulation

Figure 4.11: Time evolution of the ratio between the sink accretion radius ($r_{\rm acc}$) and core radius ($r_{\rm core}$, defined with different threshold densities) for each simulation. The *top left panel* corresponds to the simulation labeled as C100, the *top right panel* to O100, the *bottom left panel* to the C1000, and the *bottom right panel* to the O1000. The horizontal line corresponds to a value of $r_{\rm acc}/r_{\rm core} = 0.25$, so we suggest that every point above the line can be affected by numerical issues.

# Chapter 5
# Conclusions

The main objective of this work is to study how varying the accretion and the definition of the core would affect the measurements regarding the star formation efficiency (SFE) and star formation efficiency per free-fall time ($\epsilon_{ff}$).

A summary of the results given in the previous chapter is present in the following:

- A discrepancy was observed in the collapse time of simulations with different densities. The low-density simulations evolve more slowly due to thermal support providing resistance against collapse.
- Simulations with open boundary conditions (OBC) exhibit a more efficient sink accretion compared to simulations with closed boundary conditions (CBC) due to the injection of material into the numerical box and the core[1].
- In cores defined with low density thresholds, the BCs affect the values of SFE, while in cores with higher density thresholds the SFE is similar regardless of the BCs.
- The high density threshold for defining the core results in higher efficiencies, indicating that smaller cores have a larger fraction of their mass absorbed by the sink.
- High values of $\epsilon_{ff}$ are measured compared to the expected values for star-forming regions, which can be attributed to the idealizations made to quantify $\tau_{ff}$ and the assumption of a single center of collapse instead of multiple centers.

[1]This is valid for the numerical box used in this work. However, if the box size is increased, the effect will start to disappear. For a box with an infinite size $L_{\text{box}} \to \infty$, there would be no difference in the sink accretion efficiency.

- The evolution of $\epsilon_{ff}$ shows a decreasing trend with lower density thresholds, indicating the influence of core definition on the measured efficiency.

- The curves of $\epsilon_{ff}$ are nearly constant in space and time.

The previous findings lead to several important conclusions. The measured SFE of the cores is directly influenced by the chosen density threshold for defining the core, highlighting the importance of core definition and its impact on the analysis outcomes. The BCs also play an important role in determining the SFE, with simulations using open BCs giving lower values of these quantities, which is more consistent with observations.

Our analysis shows that the $\epsilon_{ff}$ is roughly constant in time. Furthermore, a simple analysis demonstrates that if the density profile follows a profile $\rho \propto r^{-2}$, then the mass and density scale proportionally with radius, then $\epsilon_{ff}$ becomes independent of radius. Thus, the $\epsilon_{ff}$ remains constant regardless of radius and time, as long as the core gets a stationary state.

In summary, this study highlights the implications of different scenarios in accretion and core definition on SFE and $\epsilon_{ff}$, emphasizing the importance of careful consideration when selecting substructures within a molecular cloud, as it directly affects the efficiency measurements. Additionally, it reveals the independent behavior of $\epsilon_{ff}$ with the BCs and its and its slight dependence on core definition.

# References

André P., Di Francesco J., Ward-Thompson D., Inutsuka S. I., Pudritz R. E., Pineda J. E., 2014, in Beuther H., Klessen R. S., Dullemond C. P., Henning T., eds, Protostars and Planets VI. pp 27–51 (arXiv:1312.6232), doi:10.2458/azu˙uapress˙9780816531240-ch002

Barnes J., Hut P., 1986, Nature, 324, 446

Binney J., Tremaine S., 1987, Galactic dynamics

Bonnor W. B., 1956, MNRAS, 116, 351

Camacho V., Vázquez-Semadeni E., Palau A., Busquet G., Zamora-Avilés M., 2020, ApJ, 903, 46

Chevance M., Krumholz M. R., McLeod A. F., Ostriker E. C., Rosolowsky E. W., Sternberg A., 2022, arXiv e-prints, p. arXiv:2203.09570

Clark P. C., Glover S. C. O., Klessen R. S., 2011, Monthly Notices of the Royal Astronomical Society, 420, 745

Clarke C., Carswell B., 2007, Principles of Astrophysical Fluid Dynamics. Cambridge University Press, doi:10.1017/CBO9780511813450

Dale J. E., 2017, MNRAS, 467, 1067

Draine B. T., 2011, Physics of the Interstellar and Intergalactic Medium

Dubey A., Antypas K., Ganapathy M. K., Reid L. B., Riley K., Sheeler D., Siegel A., Weide K., 2009, Parallel Computing, 35, 512

Dyson J., Williams D., 1980, Physics of the Interstellar Medium. Manchester University Press, https://books.google.com.mx/books?id=BHi7AAAAIAAJ

Ebert R., 1955, , 37, 217

Estalella R., Anglada G., 1999, Introducción a la Física del Medio Interestelar. Universitat de Barcelona, http://www.publicacions.ub.es/refs/indices/06905.pdf

Falgarone E., Phillips T. G., Walker C. K., 1991, ApJ, 378, 186

Federrath C., 2015, MNRAS, 450, 4035

Federrath C., Klessen R. S., 2012, ApJ, 761, 156

Federrath C., Banerjee R., Clark P. C., Klessen R. S., 2010, ApJ, 713, 269

Ferrière K. M., 2001, Reviews of Modern Physics, 73, 1031

Ferziger J., Peric M., 2001, Computational Methods for Fluid Dynamics. Springer Berlin Heidelberg, https://books.google.com.mx/books?id=1D3EQgAACAAJ

Francesco J. D., au2 N. J. E. I., Caselli P., Myers P. C., Shirley Y., Aikawa A., Tafalla M., 2006, An Observational Perspective of Low-Mass Dense Cores I: Internal Physical and Chemical Properties (arXiv:astro-ph/0602379)

Fryxell B., et al., 2000a, FLASH code user manual. University of Chicago, https://flash.uchicago.edu/site/flashcode/user_support/flash_ug_4.5.pdf

Fryxell B., et al., 2000b, ApJS, 131, 273

Girault V., Raviart P., 2012, Finite Element Methods for Navier-Stokes Equations: Theory and Algorithms. Springer Series in Computational Mathematics, Springer Berlin Heidelberg, https://books.google.com.mx/books?id=8C7vCAAAQBAJ

Gómez G. C., Vázquez-Semadeni E., 2014, ApJ, 791, 124

Gómez G. C., Vázquez-Semadeni E., Palau A., 2021, Monthly Notices of the Royal Astronomical Society, 502, 4963

Grudić M. Y., Hopkins P. F., Faucher-Giguère C.-A., Quataert E., Murray N., Kereš D., 2018, MNRAS, 475, 3511

Grudić M. Y., Hopkins P. F., Lee E. J., Murray N., Faucher-Giguère C.-A., Johnson L. C., 2019, MNRAS, 488, 1501

Hennebelle P., Inutsuka S.-i., 2019, Frontiers in Astronomy and Space Sciences, 6, 5

Jeans J. H., 1902, Philosophical Transactions of the Royal Society of London Series A, 199, 1

Kim J.-G., Ostriker E. C., Filippova N., 2021, ApJ, 911, 128

Krumholz M. R., McKee C. F., 2005, ApJ, 630, 250

Krumholz M. R., Tan J. C., 2007, ApJ, 654, 304

Krumholz M. R., McKee C. F., Bland-Hawthorn J., 2019, ARA&A, 57, 227

Lada C. J., Lada E. A., 2003, ARA&A, 41, 57

Lada C. J., Lombardi M., Alves J. F., 2010, ApJ, 724, 687

Landau L., Lifshits E., 2003, Fluid Mechanics. Teoreticheskaiafizika, Butterworth-Heinemann, https://books.google.com.mx/books?id=kV46zQEACAAJ

Li G.-X., 2018, MNRAS, 477, 4951

Louvet F., et al., 2014, A&A, 570, A15

Mac Low M.-M., Klessen R. S., 2004, Reviews of Modern Physics, 76, 125

Molinari S., et al., 2014, in Beuther H., Klessen R. S., Dullemond C. P., Henning T., eds, Protostars and Planets VI. pp 125–148 (arXiv:1402.6196), doi:10.2458/azu˙uapress˙9780816531240-ch006

Myers P. C., 1978, ApJ, 225, 380

Myers P. C., Dame T. M., Thaddeus P., Cohen R. S., Silverberg R. F., Dwek E., Hauser M. G., 1986, ApJ, 301, 398

Naranjo-Romero R., Vázquez-Semadeni E., Loughnane R. M., 2015, ApJ, 814, 48

Ochsendorf B. B., Meixner M., Roman-Duval J., Rahman M., Evans Neal J. I., 2017, arXiv e-prints, p. arXiv:1704.06965

Padoan P., Haugbølle T., Nordlund Å., 2012, ApJ, 759, L27

Palau A., et al., 2014, ApJ, 785, 42

Pillai T., Wyrowski F., Carey S. J., Menten K. M., 2006, A&A, 450, 569

Pokhrel R., et al., 2021, ApJ, 912, L19

Salmon J. K., Warren M. S., 1994, Journal of Computational Physics, 111, 136

Shu F. H., 1977, ApJ, 214, 488

Shu F. H., Adams F. C., Lizano S., 1987, ARA&A, 25, 23

Springel V., 2005, MNRAS, 364, 1105

Stahler S. W., Palla F., 2005, The Formation of Stars. Wiley-VCH

Truelove J. K., Klein R. I., McKee C. F., Holliman John H. I., Howell L. H., Greenough J. A., 1997, ApJ, 489, L179

Vázquez-Semadeni E., Palau A., Ballesteros-Paredes J., Gómez G. C., Zamora-Avilés M., 2019, MNRAS, 490, 3061

Waagan K., 2009, Journal of Computational Physics, 228, 8609

Whitworth A., Summers D., 1985, MNRAS, 214, 1

Williams J. P., Blitz L., McKee C. F., 2000, in Mannings V., Boss A. P., Russell S. S., eds, Protostars and Planets IV. p. 97 (arXiv:astro-ph/9902246), doi:10.48550/arXiv.astro-ph/9902246

Wolfire M. G., Hollenbach D., McKee C. F., Tielens A. G. G. M., Bakes E. L. O., 1995, ApJ, 443, 152

Wünsch R., Walch S., Dinnbier F., Whitworth A., 2018, Monthly Notices of the Royal Astronomical Society, 475, 3393